MECHANISMS OF SEDIMENTATION INFERRED FROM QUANTITATIVE

CHARACTERISTICS OF HEAVY AND LIGHT MINERALS SORTING AND

ABUNDANCE

A Dissertation

by

KANNIPA MOTANATED

Submitted to the Office of Graduate and Professional Studies of
Texas A&M University
in partial fulfillment of the requirements for the degree of

DOCTOR OF PHILOSOPHY

Chair of Committee,	Michael M. Tice
Committee Members,	Thomas D. Olszewski
	David Sparks
	Scott A. Socolofsky
Head of Department,	John R. Giardino

August 2014

Major Subject: Geology

ABSTRACT

Hydraulic behaviors of particles with contrasting sizes and densities and flow structure of hyperconcentrated suspensions were empirically studied in a thin vessel by using particle-image-velocimetry techniques. Particle volumetric concentration, C_v, of the suspensions were mainly affected by the majority particle species, silica ballotini. The minority population was aluminum ballotini (hydraulically fine). At high C_v, aluminum particles were less retarded and settled as if they were hydraulically coarser. This was because particles moved in a cluster-like motion. Terminal settling velocities of both particles converged at $C_v \geq 25\%$, and particle sorting was diminished.

Spatial and size distributions of mineral grains with contrasting densities in massive sandstones of turbidites from the Middle Permian Brushy Canyon Formation were used to estimate suspended sediment concentrations and interpret hydraulic evolution of the turbidity currents. Semi-quantitative elemental distributions were estimated by x-ray fluorescence analytical microscopy, µXRF. Within the structureless sandstone, zircon grains (hydraulically fine) fined upward while feldspar grain (hydraulically coarse) sizes did not change. Both grains had hydraulically equivalent settling velocities in overlying siltstone layers. These suggest that these sandstone divisions were deposited from hyperconcentrated suspensions where particle segregation was diminished and hydraulically fine grains were entrained with hydraulically coarse particles. While structureless sandstones were deposited, C_v increased through distance

and time because hydraulically fine particles were fining upward. This evolution likely be resulted from volumetric collapse of the turbidity currents.

Geochemical concentrations and properties of Zr- and Ti-rich particles were used to qualitatively estimate erosional event sizes of hemipelagic thinly laminated siltstone. Zircon and rutilated quartz particle sizes, Zr/Ti fluorescence ratio, and lamination thickness were determined by μXRF. Zircon grains were finer than rutilated quartz grains. Their grain sizes were systematically correlated but neither was correlated with Zr/Ti ratio. Instead, Zr/Ti ratio covaried with lamination thickness. Since zircon grains are smaller but heavier than rutilated quartz grains, zircon has lower susceptibility to erosion, particularly by wind. Thus, fluctuations of Zr/Ti fluorescence ratio in Brushy canyon Formation siltstones most likely result from variations in the intensity of erosional events at the particle source or sources, with high Zr/Ti ratios reflecting periods of intense erosion.

ACKNOWLEDGEMENTS

I would like to thank my committee chair, Dr. Michael M. Tice, for his advice, constructive comments, and support. I would also like to thank my committee members, Dr. Thomas D. Olszewski, Dr. David Sparks, and Dr. Scott A. Socolofsky, for their guidance and insightful knowledge throughout the course of this research. Thanks to Amanda D. Kallus and Spencer B. Gunderson for their helps in the field. Thanks also go to Jian Gong for his help on setting up the experiments. I would like to thank Prof. Dr. Peter Vennemann for his help on JPIV software. I also want to extend my gratitude to the National Parks Department for their cooperation.

Lastly, I would like to thank friends, colleagues, and the department faculty and staff for making my time at Texas A&M University a great experience.

TABLE OF CONTENTS

Page

LIST OF FIGURES

LIST OF TABLES

CHAPTER I

INTRODUCTION

Beaubouef et al. (1999) estimated that at least 90% of the Brushy Canyon Formation, Delaware Basin, west Texas and southeast New Mexico was deposited as turbidites and the rest as debrites and hemipalegites. The structureless sandstones of the Brushy Canyon Formation have been extensively researched and interpreted as fine-grained sandstones deposited by rapid fallout from turbid suspensions (Beaubouef et al., 1999). In the Upper Brushy Canyon Formation, structureless sandstones were deposited as channel infill during a relatively low sea level. Since light and heavy minerals are hydraulically sorted in sands, analysis of sediment sorting and distribution is commonly used for interpreting flow properties, mechanisms of deposition and transportation, and relative transport distance of sediments (e.g., Allen, 1991; Bowen et al., 1984; Komar, 1985; Middleton, 1976; Rubey, 1933; Slingerland and Smith, 1986; Slingerland, 1977; Steidtmann, 1982; Van Tassell, 1981; Visher, 1969).

Sedimentation processes are commonly exploited in heavy mineral separation processes in the chemical and mining industries. Theoretical and empirical studies of mechanisms of sedimentation and liquid-solid fluidization have been extensively researched and they are applicable to sedimentological problems, as well. Middleton and Southard (1984) explained the differences in mechanisms of sediment movement in infinitely dilute and concentrated suspensions. When a particle settled through a still viscous fluid, it accelerated until the upward fluid drag force was equal to the

1

gravitational force. Then, the particle would fall at a constant velocity called the terminal settling velocity. Russel et al. (1984) quantitatively studied fluid-solid and solid-solid interactions in colloidal suspensions. The study revealed that in finite volumetric sediment concentrations, terminal settling velocities were different and much more complex from those in infinitely dilute suspensions. Interactions between particles had a great influence on sedimentation. These particle interactions should be reflected in the spatial distribution of suspension. Thus, the spatial distribution of suspension during settling is critical for evaluating the relationship between sedimentation and particle volumetric concentration of suspensions. Vector maps of particle movements are, therefore, essential for understanding the sedimentation processes in highly concentrated suspensions.

The central theme of this dissertation is the use of heavy minerals as probes of depositional processes. Empirical study on settling velocities of particles with contrasting sizes and densities in hyperconcentrated suspension leads to an insightful understanding of flow structure and particle's hydraulic behaviors. The results from this chapter can be used to interpret flow evolution of turbidites. The last chapter uses the relationship between particle sizes and abundances as qualitative proxies for the intensity of erosional events of hemipelagic thinly laminated siltstone in the Brushy Canyon Formation of west Texas and south New Mexico.

1.1 ORGANIZATION

This dissertation is organized into three main chapters. Chapter II presents an experimental study of heavy mineral sorting in dense suspensions of light mineral grains, where heavy particles are the minority and the light particles are the majority populations. Chapter III analyzes hydraulic evolution of turbidity currents from high to low densities based on heavy and light mineral sorting and distribution. Chapter IV presents estimation of erosional event sizes of thinly laminated siltstone by using geochemical properties as proxies.

1.2 OBJECTIVE

The objectives of the second dissertation chapter are to use grain settling experiments conducted in a thin vessel and particle-image-velocimetry (PIV) techniques (1) to study spatial distribution and sorting of light and heavy minerals at various volumetric concentrations and (2) to analyze inter-particle and particle-fluid interactions during hindered settling as a function of volumetric concentration.

The objectives of the third chapter are (1) to detect and characterize heavy and light mineral (Zr- and K-bearing particles, respectively) sorting and distribution within structureless sandstones from the Brushy Canyon Formation, Delaware Basin, southern New Mexico and (2) to use grain size distributions of mineral grains with contrasting densities and the results from Chapter II to quantitatively describe the turbidity flow's evolution.

The objectives of the fourth chapter are (1) to detect and characterize sorting and distribution of heavy, Zr-bearing grains, and light, Ti-bearing grains, with in the thinly laminated siltstones of the Brushy Canyon Formation, Delaware Basin, southern New Mexico and (2) to use geochemical properties as proxies to qualitatively analyze sources of Zr/Ti fluorescence ratio variation.

CHAPTER II

EXPERIMENTAL CHARACTERIZATION OF HEAVY MINERAL SORTING

FROM DENSE SUSPENSIONS OF LIGHT MINERAL GRAINS

2.1 INTRODUCTION

Particles' transport and deposition processes depend on their size, shape, density, and grain support mechanisms. Gross changes in sediment concentration can produce diagnostic transitions between different types of deposits (e.g., Amy et al., 2006; Felix, 2002). Richardson and Meikle (1961) experimentally studied sedimentation and settling velocity of mixtures of equal volumes of heavy glass ballotini and light polystyrene. Amy et al. (2006) experimentally investigated sand-mud suspension settling behavior. Their research results concluded that particle segregation depended on particle volumetric concentration, C_v. However, heavy mineral grains are commonly hydraulically finer than light mineral grains in the same sediment source. The existing literature is not clear on how mixtures of these grains will settle. This research empirically studies flow structures and hydraulic behaviors of heavy particles that are hydraulically finer than light particles, at various C_v. The particle volumetric concentration of small heavy particles is low enough that they are treated like the minority particles, similar to what can be found in nature.

2.2 BACKGROUND

For particles in uniform suspensions with $C_v > 1\%$, the force resisting settling results from the velocity gradient due to the upward movement of fluid displaced by the downward movement of particles (e.g., Davis et al., 1988; Nicolai et al., 1995; Richardson and Zaki, 1954). The settling velocity of a particle in concentrated suspension is lower than its Stokes velocity because of viscosity enhancement by the surrounding particles and fluid backflow generated by the motion of nearby particles; it is well-described by Equation 2.1 (Richardson and Zaki, 1954):

$$V_{RZ} = V_S(1 - C_v)^n. \tag{2.1}$$

Here, V_{RZ} is the Richardson-Zaki particle settling velocity at volumetric concentration C_v. V_S is the Stokes velocity and n is a function of particle Reynolds number. For small particle Reynolds number, $n \approx 5$ (Nicolai et al., 1995).

Alternatively, concentrated suspensions can behave as Bingham plastics with effective yield strengths and dynamic viscosities that are functions of C_v (Julien, 1998; Julien and Lan, 1991). In this case, yield strength and dynamic viscosity of the fluid are affected by suspended sediments due to cohesion between particles, internal friction between fluid and sediment particles, turbulence, and particle-particle collisions. Consequently, hyperconcentrated mixtures of homogeneous fine grains and fluid possess an apparent yield strength, τ_y (Equation 2.2), beyond which the rate of deformation,

dv_x/dz, is linearly proportional to the excess shear stress. Yield strength, τ_y, for a mixture $(C_v > 5\%)$ and dynamic viscosity of a mixture, μ_m, and are given by

$$\tau_y \, (in \, Pa) \cong 0.1e^{3(C_v - 0.05)} \tag{2.2}$$

and

$$\mu_m \cong \mu\left(1 + 2.5C_v + e^{10(C_v - 0.05)}\right). \tag{2.3}$$

Here, μ is the dynamic viscosity of the fluid at $C_v = 0$. This mixture has an average density of $\rho_m = \rho_s C_v + \rho(1 - C_v)$, where ρ is the density of the fluid and ρ_s is the density of the particle. The settling velocity of a particle in a Bingham plastic fluid, V_{BP}, can be expressed as a function of particle diameter, d_s, and drag coefficient, C_D,

$$V_{BP} = \sqrt{\frac{4}{3}\frac{g d_s}{C_D}\frac{\rho_s - \rho_m}{\rho_m}}. \tag{2.4}$$

C_D can be written as a function of particle Reynolds, Re, and Hedstrom number $He = \frac{\rho_m d_s^2 \tau_y}{\mu_m^2}$. This can be expressed as

$$C_D = \frac{24}{Re} + \frac{2\pi He}{Re^2} + 1.5. \tag{2.5}$$

Julien's particle settling velocity, V_J, which is obtained from Equations (2.4) and (2.5), is expressed as

$$V_J = \frac{8\mu_m}{\rho_m d_s}\left\{\left(1 + \frac{\rho_m g d_s^3(\rho_s - \rho_m)}{72\mu_m^2} - \frac{\pi}{48}\frac{\rho_m \tau_y d_s^2}{\mu_m^2}\right)^{0.5} - 1\right\}. \tag{2.6}$$

In the Richardson-Zaki model, particles that are hydraulically fine will always settle slower than hydraulically coarse particles. As a result, particles that are hydraulically different will not sort and deposit together. In Julien's model, particles that are hydraulically fine can have equal or greater settling velocities than hydraulically coarse particles in fluid that is hyperconcentrated with fine grains. Particles with contrasting sizes and densities could thus be sorted and deposited together. Heavy particles are commonly smaller and have fewer abundance. This research is focused on an empirical study of the hydraulic behaviors of particles with contrasting sizes and densities at particle volumetric concentrations ranging from 5% to 25%. The results from this study could be used to analyze deposits of concentrated suspensions such as high density turbidity currents.

2.3 METHODS OF STUDY

2.3.1 Experimental Setup

This research project modifies the experimental approach of Segre et al. (2001) to study the sorting mechanisms of bimodal suspensions—particles with contrasting

sizes and densities—at various particle volume fractions, C_v. In this research, sedimentation of solid particles at different volume fractions of particles in a fluid was experimentally studied by dispersing spherical glass and aluminum particles within a glycerol-water mixture in a clear rectangular vessel (Fig. 2.1). The calculated fluid dynamic viscosity, γ_{g-w}, and the measured density, ρ_{g-w}, of glycerol-water mixture were 0.016 ± 0.002 Pa s (standard error from 44 measurements) and 1177 ± 3.31 kg m^{-3} (standard error from 4 measurements), respectively, at room temperature of 24 ± 2 ^{o}C. The vessel was 6 cm wide, 0.5 cm thick, and 30 cm high (Fig. 2.1). Two spherical particle species of lighter, larger silica and denser, smaller aluminum beads were used in this research. Silica glass beads had diameters of 90-106 µm and a density of 2.45-2.50 g cm^{-3}. Aluminum beads were originally manufactured in metallic white color, and had a diameter of 70 µm and density of 3.75 g cm^{-3}. They were then dyed black with India ink that consequently increased the aluminum beads' diameters and decreased their densities. Black aluminum beads had measured diameters of 73 ± 3 µm (standard errors from 10 measurements) and a density of 2.78 ± 0.02 g cm^{-3} (calculated from their settling velocities at infinitely dilute suspension; standard error from 31 measurements). Silica and aluminum beads are hereafter referred to as light and heavy particles based on their relative densities. Particle settling velocities at infinitely dilute suspension was determined from dropping each particle grain into the glycerol-water mixture and recorded its traveling distance and time. In an infinitely dilute suspension, silica and aluminum particles had settling velocities of 0.57 ± 0.03 and 0.27 ± 0.03 mm s^{-1}, respectively (standard errors derived from 13 and 31 measurements on silica and

aluminum particle species, respectively). Both particles' Reynolds numbers were approximately 10^{-4}. Settling experiments were divided into two parts. First, monodisperse suspension of silica beads at particle volumetric concentrations, C_v, of 5%, 10%, 15%, and 20% in order to test the validity of the experimental setup. Second, binary mixtures of silica and aluminum beads had C_v of 5%, 10%, 15%, 20%, and 25%. In every bidisperse suspension, the concentration of aluminum particle in the total concentration of solids was less than 1%. Therefore, the total particle volumetric concentration of each bidisperse suspension was mainly controlled by the amount of silica beads. Consequently, the hydraulic properties of small, dense aluminum beads in concentrated suspension were dominated by the presence of the more abundant silica beads.

Since the experiments were carried out in a confining container, the container walls could potentially retard settling (Chhabra et al., 2003; Di Felice, 1996; Machač and Lecjaks, 1995). In these experiments, the wall factor, F_w, was dependent on the ratio of particle diameter to effective container diameter because particle Reynolds number was very low (Chhabra et al., 2003). F_w of silica glass and aluminum particles, calculated by using experimental results from Machač and Lecjaks (1995), equaled 0.980-0.983 and 0.985-0.986, respectively. Therefore, the effect of confining walls on both particle species was negligible.

2.3.2 Particle-Imaging Technique

Particles were soaked in the glycerol-water mixture prior to the settling experiment in order to prevent air bubbles and particle cohesion. The vessel was

vigorously agitated in order to thoroughly mix the beads with the surrounding fluid into a homogeneous mixture. Images of particle movements at a frequency of 60 frames per second were recorded by a charge-coupled device (CCD) using a depth of field of 0.5-0.7 cm. ImageJ software was used for image processing procedures including digitization, stacking, and background color correction of still-images of particle positions (Fig. 2.2). Velocity vector maps representing magnitude and vector of grain movement were calculated by using standard particle-image-velocimetry (PIV) techniques (Fig. 2.3). Since the aluminum beads were opaque and dyed with black India ink while the glass beads were white, they were visibly distinguishable (Fig. 2.2). MATLAB was used to calculate and generate normalized velocity vector, velocity contour, and particle correlation maps from particle velocity vectors derived by JPIV (Fig. 2.4, 2.5).

Vector maps of grain movements were generated from image frames at a time interval of 5/60 or 0.083 seconds via iterative JPIV software (Fig. 2.2, 2.3). The software computed velocity vectors based on the cross-correlation of the intensity distributions over the assigned areas within the flow. In this experiment, each study area was 18 mm x 11 mm or 19 mm x 12 mm. The interrogation window and search domain were set to be 32 pixels x 32 pixels (0.69 mm x 0.69 mm) and 8 pixels x 8 pixels (0.17 mm x 0.17 mm), respectively. Horizontal and vertical velocity vector components were computed (horizontal and vertical vector spacing of 0.25 mm x 0.25 mm) at this step. Terminal settling velocities were determined when the vertical velocity fluctuation of the light particle had decayed (Fig. 2.6). Flow structures were visualized through magnitude and

direction of velocity vectors and correlation between the directions of the particles'
movement. The main objective of the experiments was to analyze the hindered settling
effects on heavy minerals as a function of volumetric concentration, C_v. Thus, particle-
particle and fluid-particle interactions were the main focuses in this study.

2.4 RESULTS

2.4.1 Terminal Settling Velocities

Terminal settling velocity of glass beads from both monodisperse and bidisperse
suspensions are compared with the hindered settling model of Richardson and Zaki
(1954) in order to test the validity of this experiment (Fig. 2.7). Terminal settling
velocities of both glass and aluminum beads at C_v of 5-25% are compared against the
existing formulas proposed by Richardson and Zaki (1954) and Julien (1998). Terminal
settling velocity of light particles in monodisperse and bidisperse suspensions are in
good agreement (within ± 1 standard error) with the predicted values from Richardson
and Zaki (1954). However, the terminal settling velocity of heavy particles (the minority
particle species) calculated from Richardson-Zaki is lower than the experimental data at
$C_v \geq 5\%$.

The terminal settling velocities of silica beads (the majority particle) are well
described by Richardson-Zaki (1954) with $n = 5.8 \pm 0.9$ (standard error for the slope of a
log-log regression of V on $1 - C_v$). The terminal settling velocities of aluminum beads
(the minority particle) has $n = 4.1 \pm 0.5$ (standard error for the slope of a log-log
regression of V on $1 - C_v$).

2.4.2 Settling Flow Structures

Quantitative changes in flow structure of the dominant grain population, light particles, are observed via frequency distributions of normalized vertical velocity of light particles at C_v = 5-25% (Fig. 2.8). At C_v = 5%, the frequency distribution plot is left-skewed where the modal population is moving relatively faster than the mean vertical velocity (+1 standard deviation from the mean velocity). At C_v = 15%, the frequency distribution plot is bimodally distributed and right-skewed; one modal population is moving relatively faster, and the other is moving slower than the mean vertical velocity (±1 standard deviation from the average velocity). At C_v = 20-25%, the frequency distribution plots are right-skewed; the population distribution is more right-skewed at high C_v, indicating that the modal population is moving slower than the mean vertical velocity at high C_v.

The product of $\hat{v}_{yl} = \frac{v_{yl} - \bar{v}_{yl}}{|\bar{v}_{yl}|}$ and $\hat{v}_{yh} = \frac{v_{yh} - \bar{v}_{yl}}{|\bar{v}_{yl}|}$ characterizes the correlation between deviations from the dominant settling velocity for light and heavy grains. When both particle species have excess vertical velocities in the same direction with respect to the majority mean, the product of $\hat{v}_{yl}$ and $\hat{v}_{yh}$ is positive, and vice versa. Contour plots of the results from this step separate areas of correlated and anti-correlated light and heavy particles (Fig. 2.5, 2.9-2.11). Heavy and light particles become more correlated as C_v increases.

At C_v = 5-15%, heavy and light particle velocities are highly correlated where the velocities of light particles are more than two standard deviations from the average velocity. Within these highly correlated regions, particles are organized into rapidly

13

moving vertical plumes separated by large slow moving clumps (Fig. 2.9, 2.10). Within

plumes and clumps, heavy and light particle velocities are generally well correlated, but

they become anti-correlated along the plume and clump boundaries. Heavy and light

particles are anti-correlated at the boundaries between fast moving plumes and slow

moving clumps. On the other hand, heavy and light particles are correlated in most areas

when C_v equals 25% (Fig. 2.5). This is because regions having light particle vertical

settling velocities that are highly deviated from the average velocity are more common

than those at low C_v (Fig. 2.5, 2.9), i.e. the sizes of plumes and clumps are larger at high

C_v, their boundaries represent less of the overall flow (Fig. 2.5).
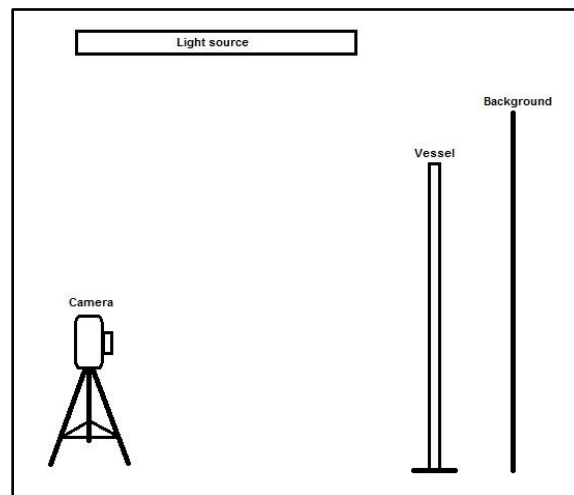
Figure 2.1 Experimental setup. The distance between the camera and the thin vessel was

9 cm where the camera's depth of field was within the depth of the vessel. The height of

the camera was adjusted so that the filming area was located away from the vessel's side

walls, the top surface of the fluid, and the sedimentation layer.
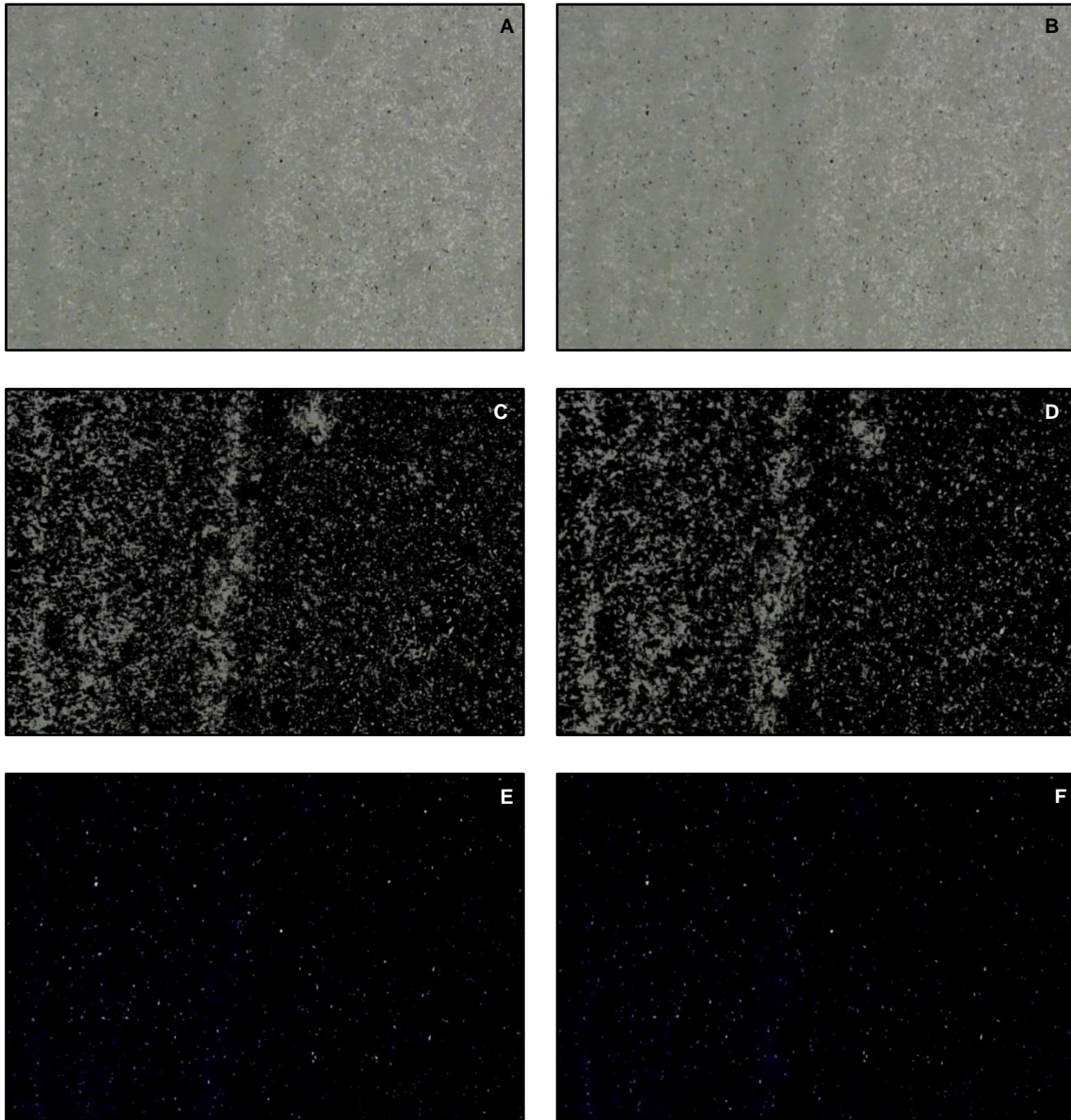
Figure 2.2 Example image pre-processing steps by ImageJ. Each image is 19 mm x 12 mm. A) An image at initial time, t_0, extracted from a video file at $C_v = 25\%$. B) An image at time $t_1 = t_0 + 0.083$ s. C) and D) Light particle images derived from A) and B), respectively. E) and F) Heavy particle images derived from A) and B), respectively.
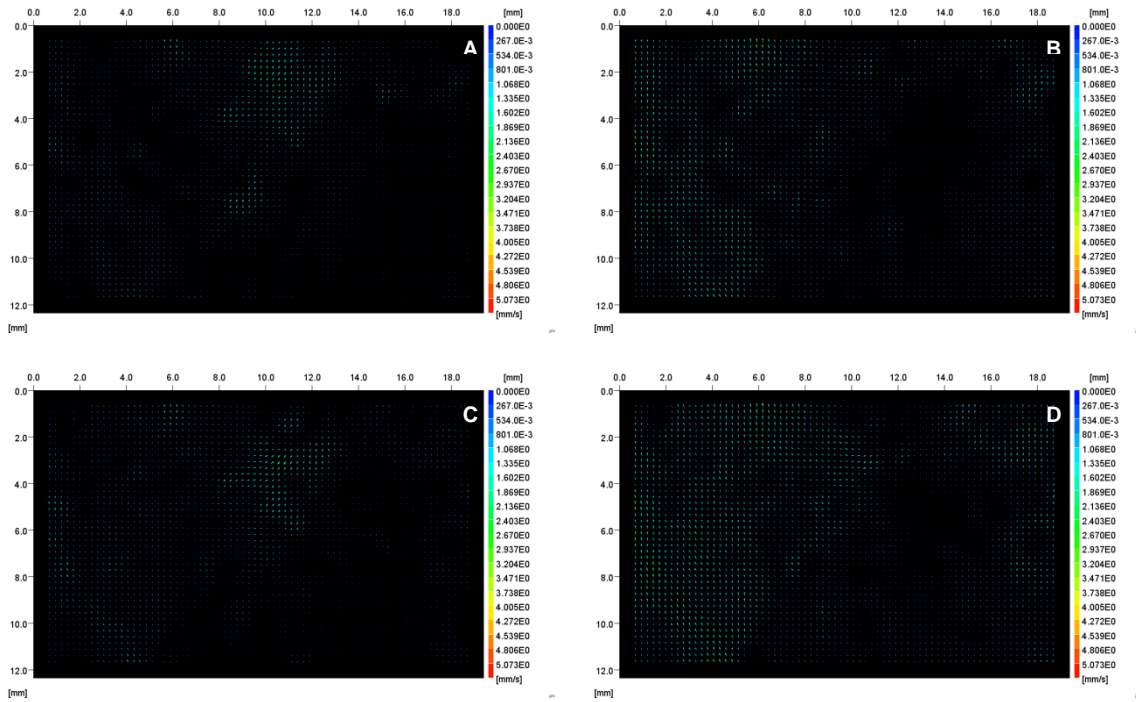
Figure 2.3 Example vector image processing steps by JPIV. A) A vector map of light particles processed from Fig. 2.2 C) and D). B) A vector map of light particles from A) subtracted by the average velocity of light particles, $v_{yl} - \bar{v}_y$. Areas where light particles move relatively slower than the average velocity have low values, vice versa. C) A vector map of heavy particles processed from Fig. 2.2 E) and F). D) A vector map of heavy particles from C) subtracted by the average velocity of light particles, $v_{yh} - \bar{v}_y$.

16
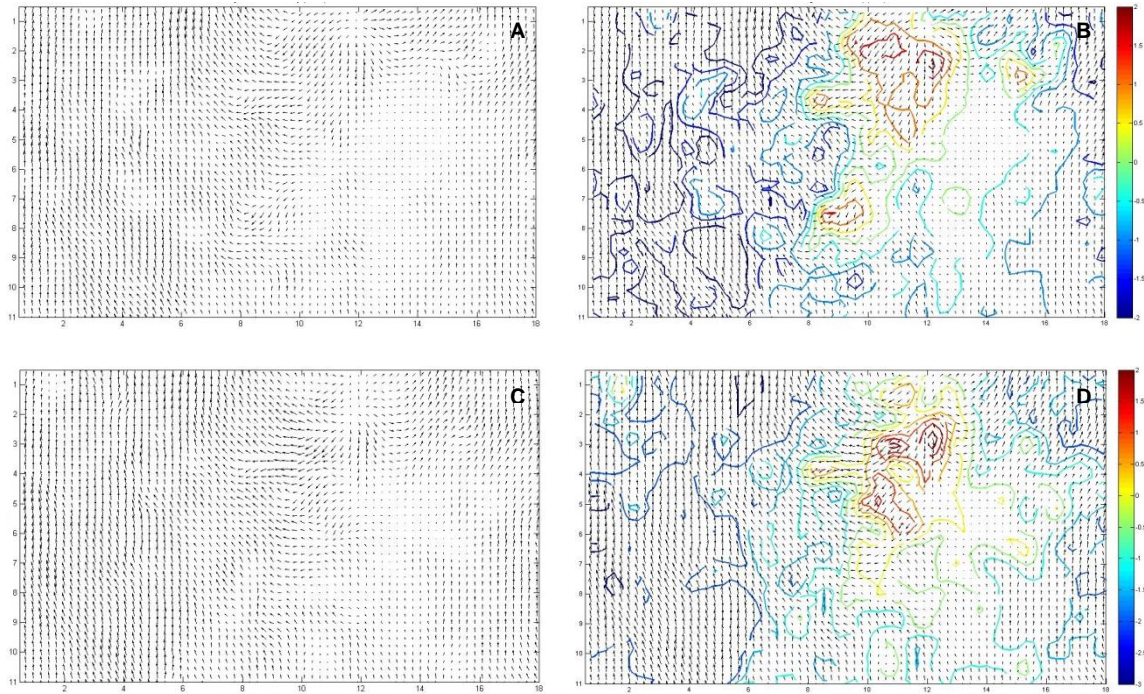
Figure 2.4 Example vector and vector contour maps processed by MATLAB. Each image is 18 mm x 11 mm. A) A velocity vector map of light particles from Fig. 2.3 B) plotted by MATLAB. B) The velocity vector map from A) overlaid by contour lines of normalized vertical velocity of light particles, $\hat{v}_{yl} = v_{yl} - \bar{v}_{yl}/|\bar{v}_{yl}|$. Areas where particles moved relatively slower than the average velocity have negative values, vice versa. C) A velocity vector map of heavy particles from Fig. 2.3 D) plotted by MATLAB. D) The velocity vector map from C) overlaid by contour lines of normalized vertical velocity of heavy particles, $\hat{v}_{yh} = v_{yh} - \bar{v}_{yl}/|\bar{v}_{yl}|$.

17
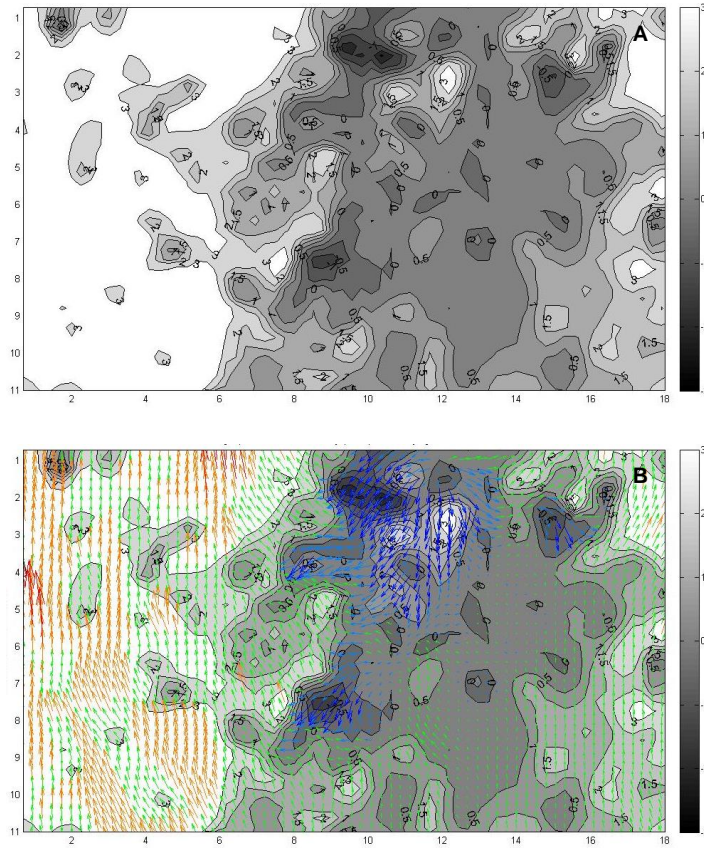
Figure 2.5 A) Example correlation between vertical velocity of light and heavy particles

from Fig. 2.4 A) and C) is presented by the product of $\hat{v}_{yl} = v_{yl} - \bar{v}_{yl}/|\bar{v}_{yl}|$ and

$\hat{v}_{yh} = v_{yh} - \bar{v}_{yl}/|\bar{v}_{yl}|$. Areas where both light and heavy particles moved relatively

faster or slower than the average vertical velocity of the light particles, $\bar{v}_{yl}$, have positive

values, correlated. Areas where one particle species moved relative slower than $\bar{v}_{yl}$ and

the other particle species moved relatively faster than $\bar{v}_{yl}$ result in negative values, anti-

correlated. B) Fig. 2.4 A) overlaid by Fig. 2.5 A). All vectors are grouped and colored

according to the standard deviation, σ, of the normalized velocity vector data into five

groups (1) red: $v_{yl} - \bar{v}_y \leq -2\sigma$, (2) orange: $-2\sigma < v_{yl} - \bar{v}_y < -\sigma$, (3) green: $-\sigma \leq$

$v_{yl} - \bar{v}_y \leq \sigma$, (4) light blue: $\sigma < v_{yl} - \bar{v}_y < 2\sigma$, and (5) dark blue $v_{yl} - \bar{v}_y \geq 2\sigma$.

18
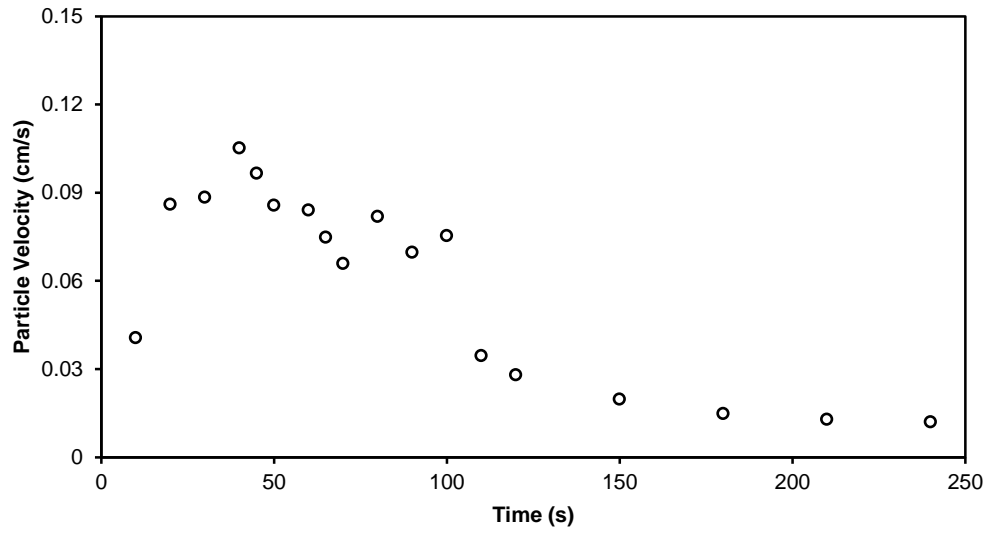
Figure 2.6 Example particle velocity (cm s^{-1}) with respect to time (s) at C_v = 20%.

Velocity fluctuation decayed at time $\geq$ 100 s.
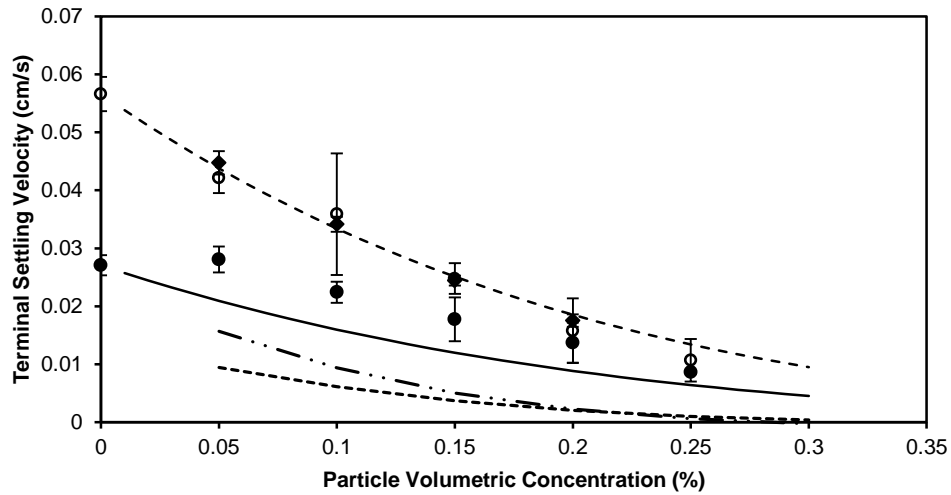
Figure 2.7 Terminal settling velocities of glass and aluminum beads at different suspended sediment concentrations. Error bars are $\pm$ 1 standard error of the mean for 3-5 experiments at $C_v > 0$ or 13-31 experiments at $C_v = 0\%$. The lower limit of the bulk rheology model is at $C_v = 5\%$. ($\circ$ = glass beads in bimodal suspension; $\bullet$ = aluminum beads in bimodal suspension; - - - = Richardson-Zaki settling velocity for glass beads; = Richardson-Zaki settling velocity for aluminum beads; - ·· - = bulk rheology model for glass beads; --- = bulk rheology model for aluminum beads; $\blacklozenge$ = glass beads in monodisperse suspension).
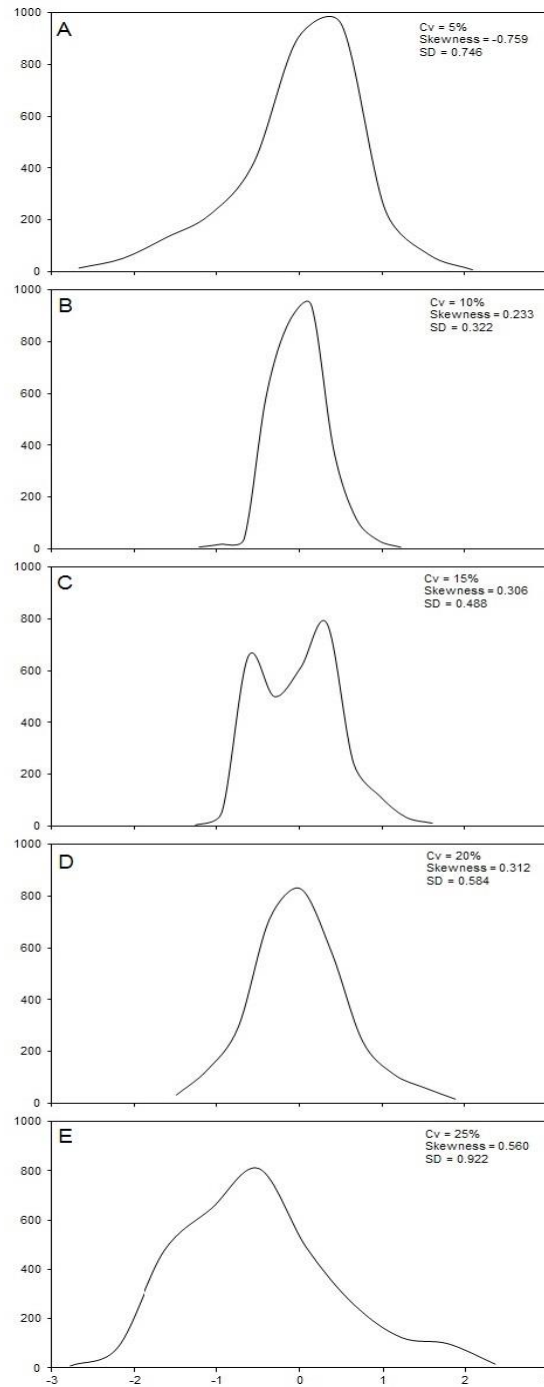
Figure 2.8 Frequency distributions of normalized vertical velocities of light particles at C_v = 5-25%. Majority population velocities shift from left skewed to right skewed, and modal velocity decreases as suspended particle concentrations increase.
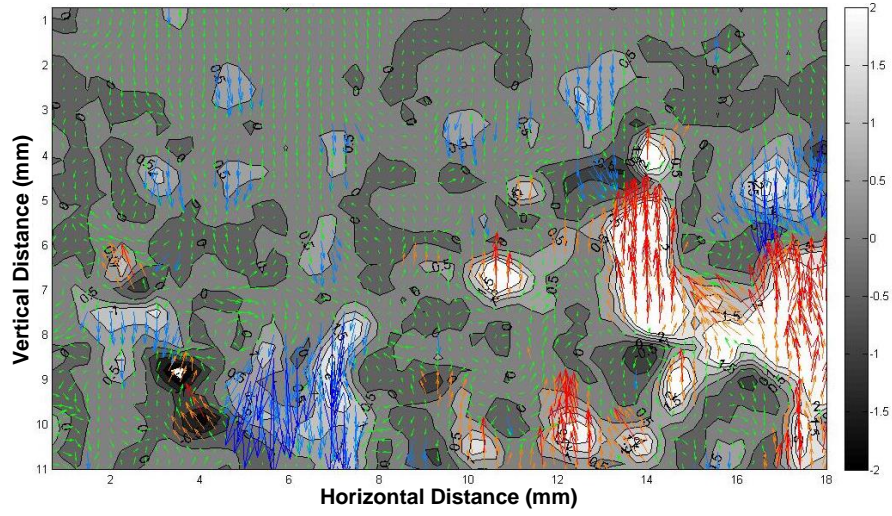
Figure 2.9 Normalized velocity vector map overlaid by contour map of light-heavy

vertical velocity correlation at $C_v = 5\%$. Vertical velocity vector component of light

particle species, v_{yl}, are normalized with respect to the average vertical velocity

component of the light particle, $\bar{v}_{yl}$. All vectors are grouped and colored according to the

standard deviation, σ, of the normalized velocity vector data into five groups (1)

$v_{yl} - \bar{v}_y \leq -2\sigma$, (2) $-2\sigma < v_{yl} - \bar{v}_y < -\sigma$, (3) $-\sigma \leq v_{yl} - \bar{v}_y \leq \sigma$, (4) $\sigma <$

$v_{yl} - \bar{v}_y < 2\sigma$, and (5) $v_{yl} - \bar{v}_y \geq 2\sigma$.
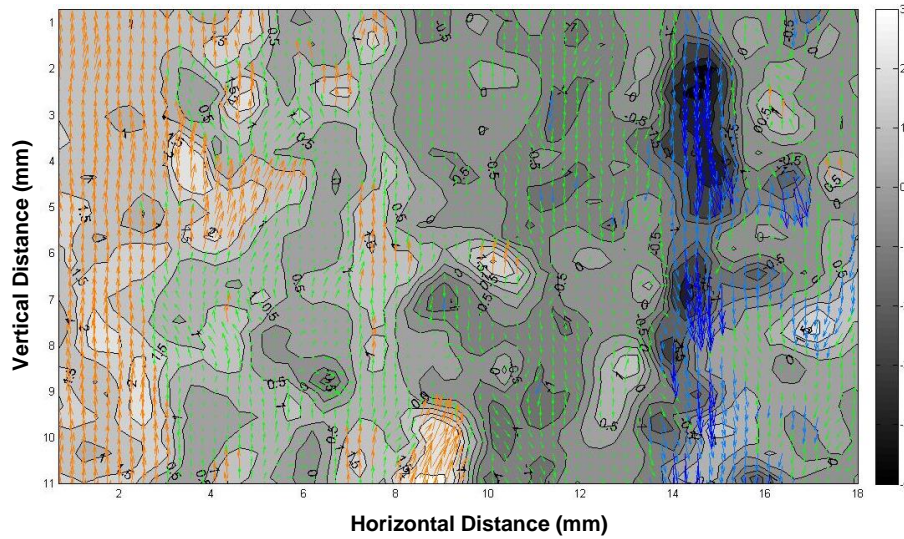
Figure 2.10 Normalized velocity vector map overlaid by contour map of light-heavy vertical velocity correlation at $C_v = 15\%$. Vertical velocity vector component of light particle species, v_{yl}, are normalized with respect to the average vertical velocity component of the light particle, $\bar{v}_{yl}$. All vectors are grouped and colored according to the standard deviation, σ, of the normalized velocity vector data into five groups (1) $v_{yl} - \bar{v}_y \leq -2\sigma$, (2) $-2\sigma < v_{yl} - \bar{v}_y < -\sigma$, (3) $-\sigma \leq v_{yl} - \bar{v}_y \leq \sigma$, (4) $\sigma < v_{yl} - \bar{v}_y < 2\sigma$, and (5) $v_{yl} - \bar{v}_y \geq 2\sigma$. Example of elutriation effect can be observed at the horizontal distance of 14-15 mm. In these areas, heavy and light particles are anti-correlated, and downward moving light particles caused relative slower, than $\bar{v}_{yl}$, moving heavy particles.

23
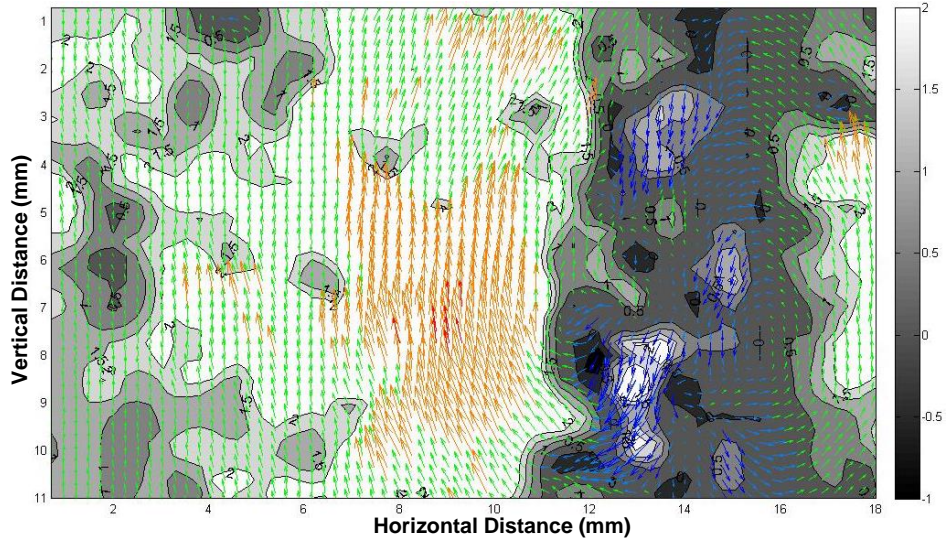
Figure 2.11 Normalized velocity vector map overlaid by contour map of light-heavy vertical velocity correlation at $C_v = 20\%$. Vertical velocity vector component of light particle species, v_{yl}, are normalized with respect to the average vertical velocity component of the light particle, $\bar{v}_{yl}$. All vectors are grouped and colored according to the standard deviation, σ, of the normalized velocity vector data into five groups (1) $v_{yl} - \bar{v}_y \leq -2\sigma$, (2) $-2\sigma < v_{yl} - \bar{v}_y < -\sigma$, (3) $-\sigma \leq v_{yl} - \bar{v}_y \leq \sigma$, (4) $\sigma < v_{yl} - \bar{v}_y < 2\sigma$, and (5) $v_{yl} - \bar{v}_y \geq 2\sigma$.
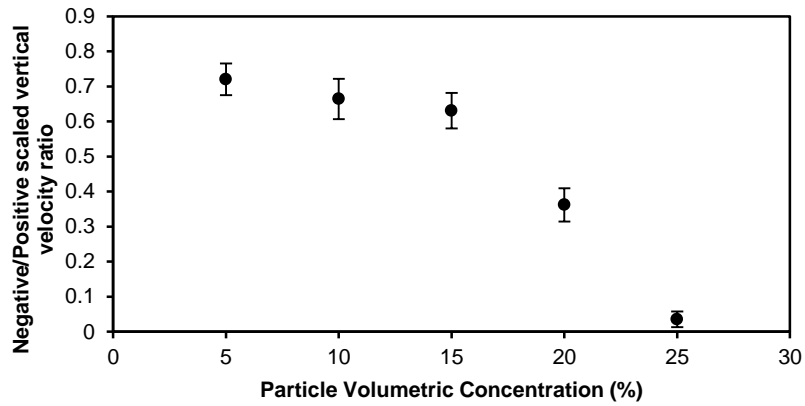
Figure 2.12 Ratio of total area with negative light-heavy velocity correlation to total area with positive light-heavy velocity correlation with respect to particle volumetric concentration, C_v. Decreasing ratio reflects organization of the settling flow into increasingly large clumps.
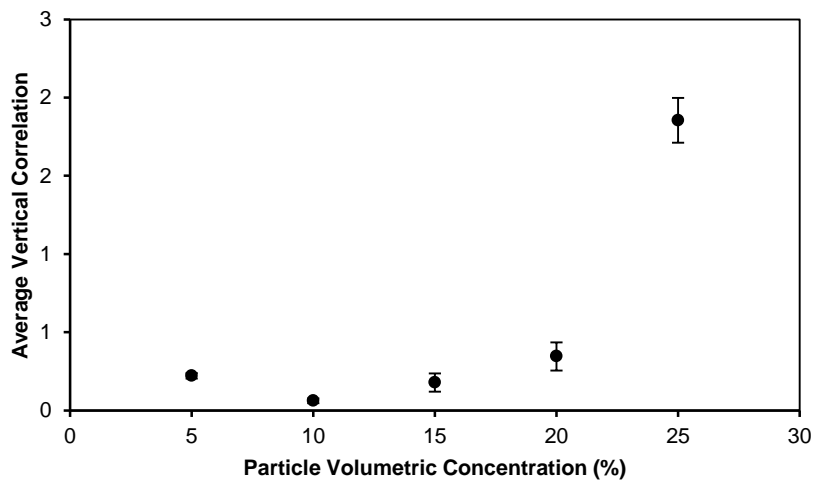
Figure 2.13 Average light-heavy correlation increases as C_v increases above 10%.
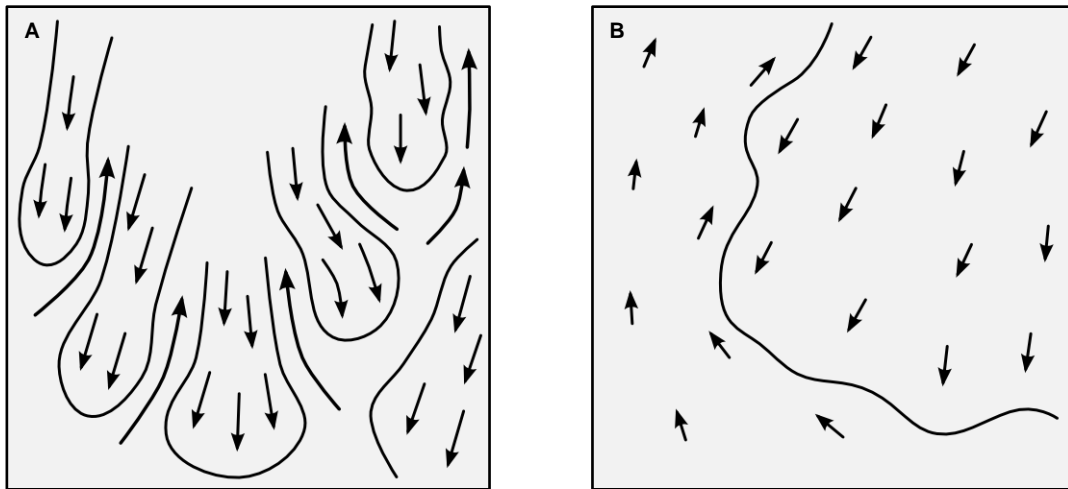
Figure 2.14 Rapidly moving vertical plumes are separated by large slow moving clumps. Within plumes and clumps, heavy and light particle velocities are generally well correlated, but they become anti-correlated along the plume and clump boundaries. A) At C_v = 5-15%, plumes and clumps are smaller and the boundaries between these two regions represent a large part of the overall flow. B) At C_v = 20-25%, plumes and clumps are larger and their boundaries represent less of the overall flow.

2.5 ANALYSIS AND DISCUSSION

2.5.1 Terminal Settling Velocities

In the present study, volumetric concentration of the small heavy particles is low enough that the hydrodynamic hindrance of small, heavy on large, light particles is assumed to be negligible. Therefore, in the case of bidisperse suspension where C_v is mainly affected by the abundance of one species, the Richardson-Zaki terminal velocity approximation is applicable for the dominant particle species. Light mineral settling velocity curve is identical to the prediction from the Richardson-Zaki model (Fig. 2.7),

and $n_l = 5.82 \pm 0.89$ (95% confidence interval), which is similar to what has been observed by other investigators, a Richardson-Zaki exponent of 5 (e.g., Nicolai et al., 1995; Segre et al., 2001).

In contrast, heavy particle velocities in bidisperse suspensions are not well-fitted by the prediction from Richardson-Zaki model. In particular, the heavy particle velocity under infinite dilute conditions is low compared to the predicted value from the fitted line (of heavy particle's settling velocities in this study). To test the categorical effect between heavy particle's settling velocity at $C_v = 0$ and at $C_v > 0$, a dummy variable (qualitative explanatory variable), $X_{dilute} = 1$ if $C_v = 0$ and 0 otherwise, was added to the regression. The regression coefficient of the dummy variable was significantly different from 0 ($p = 0.045$). Also, this regression fit yielded an n exponent of 4.84 ± 1.18 (95% confidence interval) and an R-squared value of 0.986. This evidence shows that heavy grains behave coarser at even low C_v and are not as hindered with increasing C_v as the Richardson-Zaki model predicts.

Settling velocities predicted from estimated bulk rheological properties (Julien and Lan, 1991) are systematically lower than those observed in experiments. However, the rheology model predicts that the settling velocities of light and heavy particles converge at $20\% < C_v < 25\%$, and when C_v is greater than 25%, the heavy particles settle faster than the light particles. Convergence of velocities (within measurement error) is observed in this study at $20\% < C_v < 25\%$. Observations do not extend beyond $C_v > 25\%$ because heavy particles were no longer distinguishable by the methods used here.

Therefore, C_v where hydraulically fine settle faster than hydraulically coarse particles were not observed in this study.

2.5.2 Settling Flow Structures

The ratio of anti-correlated to correlated light-heavy particles is dependent on particle volumetric concentration, C_v (Fig. 2.12). As particle volumetric concentration increases, heavy and light particles become more correlated, and vice versa. The normalized light-heavy correlation also increases when C_v increases (Fig. 2.13). This is because at low C_v the mean distance between particles is high which results in a low probability of particle-particle collision (Bagnold, 1962). Thus, particle-particle interaction is not significant. As light particles form fast moving plumes and slow moving clumps, heavy particles in both areas move relatively slower than light particles because aluminum grains are hydraulically finer in an infinitely dilute suspension. Additionally, when particle-particle interlocking is diminished, downward-moving plumes of hydraulically coarse particles could cause relatively upward elutriation of hydraulically fine particles (Davies, 1968) (Fig. 2.10). Therefore, at low C_v, up to 40% of light and heavy particles are anti-correlated, and terminal settling of heavy particles is significantly slower than that of light particles.

Bagnold (1962) proposed that when $C_v \geq 9\%$, the mean distance between particles is equal or less than their diameter resulting in a significant probability of particle collision. Thus, particle-particle interaction is dominant. In this study, at high C_v, particles settle primarily in clumps and particle suspension microstructures are important (Nicolai et al., 1995). Settling flow structures observed at 25% C_v show that the majority

of light and heavy particles are correlated because they are interlocked (Fig. 2.5). The difference in vertical velocity between the fast moving plumes and slow moving clumps is not as high as those observed at low C_v. Upward elutriations of hydraulically fine particles are not observed which are similar to the empirical results of binary and tertiary suspensions from Davies (1968). In that study, segregation of particles with equal density but different sizes vanishes at concentrations higher than their critical interlocking concentrations. Above these values, particle interlocking becomes dominant and the upward elutriation of hydraulically fine particles is diminished. These limiting values are dependent on particle size and shape and concentration of the total and each species.

In this study, when particle volumetric concentration is high, both particle species are interlocked and hydraulically fine aluminum particles are entrained with hydraulically coarse silica particles. This behavior is similar to that observed by Hoyos et al. (1994). In the suspension of noncolloidal bidisperse glass beads, large particles are hindered while small particles are 'dragged along' due to the geometric limitations of interlocking particles.

The settling velocity of the light particles (the majority population) is well-predicted by the model from Richardson and Zaki (1954). However, this model underestimates the terminal settling velocities of heavy particles (the minority population) at high C_v. This is because this model does not treat particles with contrasting sizes and densities differently. As a result, settling velocities of heavy and light particles never converge according to this model.

29

The rheology model from Julien (1998) underestimates the terminal settling velocities of both particle species. However, this model predicts that the settling velocities of heavy and light particles converge when $20\% < C_v < 25\%$, which is similar to the results found in this research. Nevertheless, at $C_v \geq 25\%$, the rheology model predicts that heavy particles settle faster than light particles. If this is the case, in hyperconcentrated suspension, heavy particles tend to accumulate at the bases of the deposits and are overlaid by a mixture of heavy and light particles, assuming the overall particle concentration of the flow is decreasing through time. Based on the results found in this research, at high C_v, the settling velocities of heavy and light particles converge but are unlikely to crossover. This is because heavy particles are entrained by light particles in clumps rather than settling between them.

2.6 CONCLUSIONS

This research demonstrated that at high particle volumetric concentration, $20\% < C_v < 25\%$, terminal settling velocities of hydraulically light and heavy particles converge but are unlikely to crossover. At high C_v, particle segregation was diminished because particles settle in clumps and hydraulically fine particles (the minority species) were trapped in locally dense clusters of hydraulically coarse particle (the majority species). Within these clusters of fast moving plumes and slow moving clumps, both particle species were moving coherently while they moved oppositely along the clusters' boundaries. As C_v increases, the difference in vertical velocity between the fast moving plumes and slow moving clumps was not as high as those observed at low C_v. Numbers

of clumps and jets were also decreasing and clumps' sizes were increasing (Fig. 2.14).

Consequently, hydraulically different particles settled together at high C_v, and particle

segregation was diminished. This result can be used to interpret volumetric

concentration and hydraulic evolution of turbidites where hydraulically different grains

coexist.

CHAPTER III

HYDRAULIC EVOLUTION OF TURBIDITY CURRENTS FROM HIGH TO LOW

DENSITIES

3.1 INTRODUCTION AND BACKGROUND

Transformations in sediment gravity flows as they move down slopes are critical in determining the architectures of submarine depositional systems. These transformations are driven by changing suspended sediment concentrations and consequent changes in grain support mechanisms (e.g., Haughton et al., 2009; Mulder and Alexander, 2001). As suspended sediment concentration increases from 1% to 9%, the mean distance between suspended grains decreases from four particle diameters to one particle diameter (Bagnold, 1962). As a result, particle-particle interactions become more frequent and more important in maintaining particles in suspension. In low-concentration turbidity currents, turbulence is the main particle support mechanism (Haughton et al., 2009; Mulder and Alexander, 2001), and sediment support is independent of particle concentration (Lowe, 1982). In high-concentration turbidity currents, turbulence, grain-grain interactions, and fluid escape are the dominant support mechanisms. Formation of bed forms is suppressed in such flow, resulting in deposits without current structures such as Bouma T_a/ Lowe S_3 divisions (Bouma, 1962; Lowe, 1982).

Because transport and deposition processes depend on grain support mechanisms, gross changes in sediment concentration produce diagnostic transitions

between different types of deposits. In other words, turbidity currents are controlled by suspended sediments (Felix, 2002) and their hydraulic properties are also recorded in sediment deposits (e.g., Kneller and McCaffrey, 2003; Komar, 1985). However, changes in concentration that do not result in changes in flow type are more difficult to diagnose in deposits, making investigation of the mechanics of flow transformation challenging.

Naturally occurring heavy minerals can be used as tracer particles because particles with contrasting sizes and densities settle differently under various volumetric concentrations (Chap. 2). Since particles are hydraulically sorted according to their transportability, which is a function of size, shape, and density, settling behavior of bimodal suspensions has been a subject of continued interest (e.g., Amy et al., 2006; Berthault, 1988; Steidtmann, 1982). Experimental investigation of settling behavior of sand-mud suspension found five distinct deposits ranging from particle size segregation to no size segregation (Amy et al., 2006). Each deposit is associated with different settling regimes that result from changes in sediment concentration. A similar study of bimodal mixtures between relatively dense ballotini and light polystyrene (equal Stokes velocities and volumes) found that at particle volumetric concentration, C_v, higher than 15%, light particles remained in suspension until heavy particles had completely settled. At C_v below 8%, there was no sediment segregation, both particles settled together (Richardson and Meikle, 1961). However, a more universal threshold concentration boundary is not clearly defined due to the complexity of factors such as particle sizes, densities, and distributions (e.g., Mulder and Alexander, 2001).

This study uses zircon and feldspar grains as test particles to investigate changing suspended sediment concentrations during deposition of T_a divisions of turbidites from the Middle Permian Brushy Canyon Formation, Eddy County, southwest New Mexico. More than 90% of the sandstones of the Brushy Canyon Formation were deposited as turbidites (Beaubouef et al., 1999). Suspension deposits such as structureless beds, climbing ripples, ripples, and plane parallel laminae settled from sandy turbidity currents. The structureless sandstone samples were deposited so rapidly that bedload structures were not existent. Thus, particle volumetric concentration of the flow at the time of deposition was preserved in these sandstones.

3.2 METHODS OF STUDY

Four slabbed rock samples were collected from T_a division sandstones as well as overlying and underlying siltstones from a core sample from the Big Eddy Field, Eddy County, New Mexico. In order to ensure analysis of complete beds, only structureless sandstones bounded above and below by other deposits, usually finely laminated siltstones representing Bouma T_d or T_a divisions, were collected (Fig. 3.1). X-ray fluorescence (XRF) microscopy (Horiba XGT-7000 X-ray Analytical Microscope) was used to map elemental distributions and grain size distributions in both sandstone and capping siltstone layers. Zircon and potassium feldspar grains were mapped by integrated Zr and K $K_{\alpha 1}$ fluorescence intensities. Fluorescence data were gathered from 100 μm scanning resolution and 51.2 mm x 51.2 mm scanning areas. Several evenly spaced 10 μm scanning resolution and 5.12 mm x 5.12 mm scanning areas from the

34

bases to the tops of massive sandstone and siltstone samples were collected to measure mineral particle sizes and distributions. XRF scanning results were analyzed using ImageJ software.

Major and minor axes of zircon and feldspar grains were measured as the full width at half maximum fluorescence intensity (background subtracted) measured across grain transects. Grains were selected for measurement by digitally overlaying grids having cell spacing twice the diameter of the largest grains and measuring the single grain closest to each node. Since flat or elongate grains have significantly different fall velocities than spherical grains of identical volume, grain shape was quantified by the Riley Sphericity ψ_r (Riley, 1941). Grains with ψ_r less than 0.69 were not included in estimates of fall velocity distributions.

3.3 RESULTS

3.3.1 Zircon Abundance Trends

Sampled structureless sandstone layers had thicknesses of 5-10 cm (Fig. 3.1). Traction carpets and bedload structures were absent in structureless sandstone samples. Zr fluorescence gradually decreased in abundance from the bases to the tops of structureless sandstone sections, dramatically decreasing, and then abruptly increasing into soft-sediment-deformed black siltstone layers. Zircon abundance had its minimum in the structureless sandstone layers at the contact between the top of the structureless sandstone and the overlying siltstones while potassium feldspar abundance stayed

35

relatively constant in the structureless sandstone and increased upward in the overlying

black siltstone layer.

3.3.2 Grain Sorting and Grading

Both zircon and feldspar populations had log-normally distributed grain sizes

(Fig. 3.2). In all four samples, light minerals had grain diameters ranging from coarse

silt-sized to fine sand-sized and heavy mineral grain sizes ranged from medium silt-sized

to very fine sand-sized. In other words, within the structureless sandstone, light minerals

were roughly about twice the size of heavy minerals. Average zircon diameters from

Bass 6111.5 core slab in the overlying soft-sediment-deformed black siltstone ($4.24 \pm$

0.25ϕ, standard error derived from 38 grains) and the adjacent structureless sandstone

($4.29 \pm 0.28 \phi$, standard error derived from 51 grains) were statistically indistinguishable

($t(87) = 0.858$; two-tail $p = 0.393$). However, average grain sizes of potassium feldspar

in the siltstone layer ($3.82 \pm 0.41 \phi$, standard error derived from 88 grains) were

significantly smaller (two-tail $p = 0.001$) than those in the structureless sandstone layer

($3.58 \pm 0.58 \phi$, standard error derived from 97 grains). The structureless sandstone

section was well sorted and the average particle sizes within the soft-sediment-deformed

black siltstone were significantly smaller than the underlying sands.
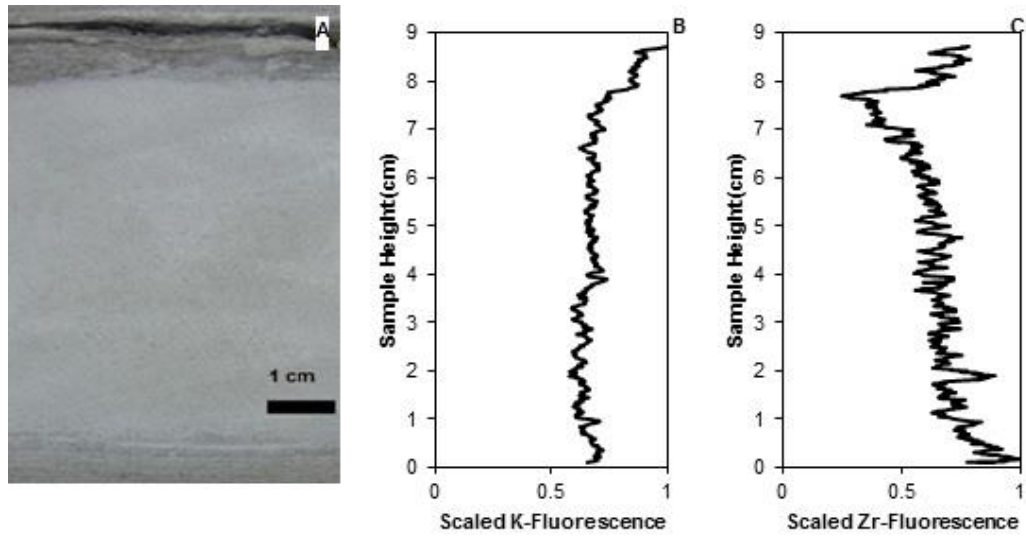
Figure 3.1 A) Structureless sandstone sample bounded above by 1-cm-thick soft-sediment-deformed black siltstone and below by 1-cm-thick thinly laminated siltstones. B) and C) Normalized K fluorescence and Zr fluorescence profiles, respectively, to represent feldspar and zircon distributions with respect to height above the lower siltstone. Within the structureless sandstone section, K fluorescence remains relatively constant while that of Zr decreases upward.
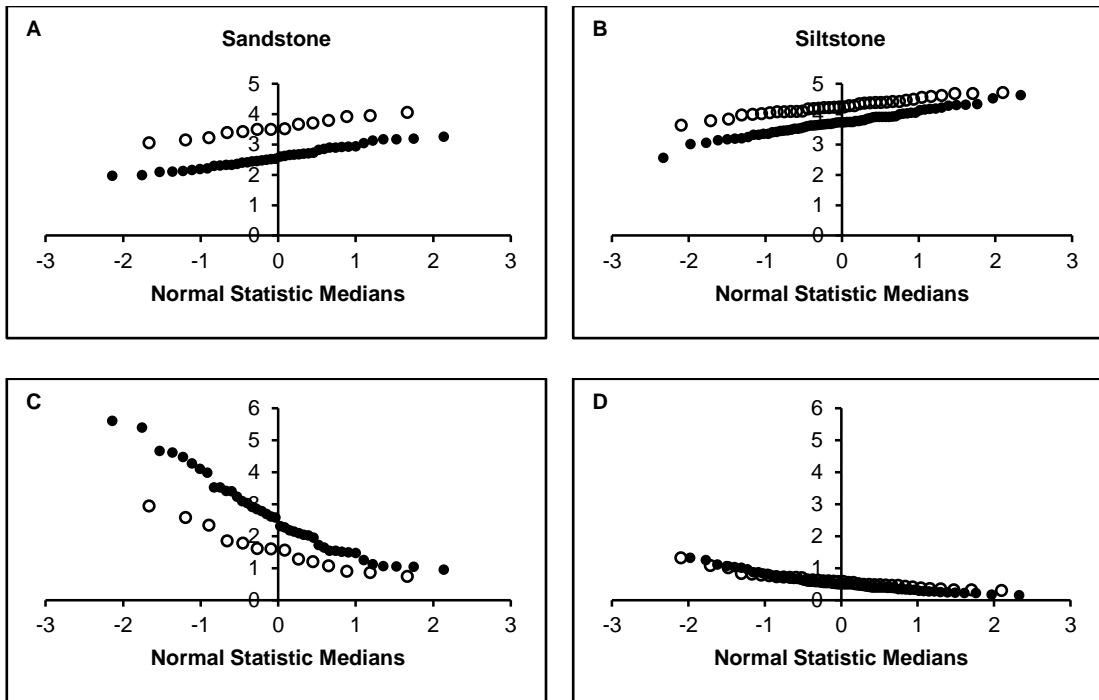
Figure 3.2 Normal probability plots of grain sizes (phi) and settling velocities at infinite dilution for feldspar (•) and zircon (○) grains. A) and B) Normal probability plots of light and heavy grain diameters (phi) of the massive sandstone and the overlying black siltstone, respectively. C) and D) Stokes setting velocities (cm s^{-1}) at infinite dilution of light and heavy particles in the massive sandstone and the overlying black siltstone, respectively. Heavy and light populations in siltstone are hydraulically equivalent while those of sandstones are not, referred to panels D and C, respectively.

Table 3.1 Paired sample t-tests of Zr- and K-rich grain sizes.

Sample	Minerals	Grain Diameter (phi)	Positions	t-value[†]	p-value
		Base: 4.30 ± 0.03	Base-Mid	t(116) = -0.504	0.615
	Zr	Mid: 4.33 ± 0.04	Mid-Top	t(116) = -0.468	0.640
		Top: 4.35 ± 0.03	Base-Top	t(116) = -1.346	0.181
Bass6100		Base: 3.32 ± 0.05	Base-Mid	t(116) = 1.544	0.125
	K	Mid: 3.20 ± 0.05	Mid-Top	t(116) = 0.532	0.596
		Top: 3.16 ± 0.05	**Base-Top**	t(116) = 2.260	**0.026***
		Base: 4.38 ± 0.04	Base-Mid	t(69) = -1.166	0.248
	Zr	Mid: 4.44 ± 0.05	Mid-Top	t(69) = -1.186	0.240
		Top: 4.52 ± 0.05	**Base-Top**	t(69) = -2.204	**0.031***
Bass6111 Section 1		Base: 3.63 ± 0.06	Base-Mid	t(69) = 0.904	0.369
	K	Mid: 3.57 ± 0.06	Mid-Top	t(69) = -1.082	0.283
		Top: 3.66 ± 0.06	Base-Top	t(69) = -0.320	0.750
		Base: 4.25 ± 0.04	**Base-Mid**	t(75) = -3.854	**0.000***
	Zr	Mid: 4.46 ± 0.04	Mid-Top	t(75) = 0.714	0.477
		Top: 4.42 ± 0.04	**Base-Top**	t(75) = -3.008	**0.004***
Bass6111 Section 2		Base: 3.62 ± 0.05	Base-Mid	t(75) = 1.909	0.060
	K	Mid: 3.47 ± 0.05	Mid-Top	t(75) = -1.260	0.212
		Top: 3.57 ± 0.07	Base-Top	t(75) = 0.493	0.624
	Zr	Base: 3.19 ± 0.09 Top: 3.55 ± 0.08	**Base-Top**	t(113) = -3.719	**0.003***
Bass6111 Section 3	K	Base: 2.76 ± 0.09 Top: 2.67 ± 0.07	Base-Top	t(113) = 0.810	0.433

[*]Sample pairs with grain populations having different average diameters at the 95%
confidence interval or greater shown in bold.

[†]The degrees of freedom are in parentheses.

Table 3.2 Two-way repeated measures analysis of variance of grain size for zircon and
feldspar grain sizes.

Sample	Source	p-value
	Mineral	0.000
Bass 6100	Position	0.483
	Mineral*Position	**0.025***
	Mineral	0.000
Bass 6111 Section 1	Position	0.304
	Mineral*Position	0.325
	Mineral	0.000
Bass 6111 Section 2	Position	0.524
	Mineral*Position	**0.001***
	Mineral	0.000
Bass 6111 Section 3	Position	0.118
	Mineral*Position	**0.026***

*Samples with mineral type and sample height interaction at the 95% confidence interval
or greater shown in bold.

Zircon grains were normally graded while feldspar grains were normally graded
in three out of four sampled beds (Table 3.1). Additionally, feldspar grains were
inversely graded in the other sample. Two-way repeated measures analysis of variance
(ANOVA) for grain size with mineral type and sample height as independent factors
showed that three out of four samples had a statistically significant interaction between
mineral and position (Table 3.2). Thus, zircon and feldspar grains grade with respect to

each other within the sandstone beds, with zircon grains fining relative to the feldspar grains.

Thus, within the structureless sandstones (1) both heavy and light minerals were well-sorted, (2) potassium feldspar grain sizes did not vary significantly, and (3) zircon grains were normally graded. Feldspar grains in siltstones were finer than those in adjacent sandstones, and zircon grain sizes were not different. Additionally, within overlying soft-sediment-deformed black siltstones, zircon and feldspar grains had equal calculated terminal fall velocities at infinitely dilute suspension (Fig. 3.2D). Stokes settling velocities of feldspar grains in the sandstones were approximately twice those of co-occuring zircon grains, while calculated settling velocities of feldspar grains in siltstones were about the same as those of zircon.

3.4 ANALYSIS AND DISCUSSION

Because heavy and light minerals are hydraulically sorted and behave differently under different flow conditions, it is possible to estimate a concentration in the depositional region at which hydraulically fine heavy mineral grains settle with hydraulically coarse light mineral grains in order to form these structureless sandstones. In this study, settling velocities of light and heavy minerals estimated by models from Richardson and Zaki (1954), Julien (1998), and Chapter II are compared against each other. These estimates are further used to deduce volumetric concentration of turbidity current at the time that the structureless sandstones were deposited.

41

Terminal settling velocities based on Richardson and Zaki's model show that potassium feldspar particles always have faster terminal velocities than zircon particles at every C_v. This is because, under Richardson and Zaki's model, both heavy and light particles are affected identically by increasing C_v. Thus, Richardson and Zaki's model is not suitable for examining differential settling of particles with contrasting sizes and densities. For Julien's model, settling velocities of zircon grains identified in this study are equal to or greater than those of potassium feldspar grains at $C_v \geq 0.25$. This crossover is an effect of an apparent yield stress that increases with increasing C_v. The Bingham plastic model is more applicable to homogeneous suspensions of fine grains (Julien, 1998) while this study is concentrated on settling characteristics of the finest grains in a flow. Julien's model was not purposely created for polydisperse suspension of particles with contrasting sizes and densities. Nonetheless, Julien's model suggests that it is possible to have heavy fine particles settling with light large particles under hyperconcentrated suspension, which agrees with recent settling experiments (Chap. 2) where hydraulically finer heavy grains were entrained into settling clumps by majority light grains. Moreover, the C_v at which settling velocities converge is the same as that observed in experiments (Chap. 2). It therefore seems likely that these structureless sandstones were deposited when the particle volumetric concentration of the turbidity currents was at least 20-25%.

Because zircon grains fined upward relative to feldspar grains, their settling velocities at infinite dilution would have become increasingly disparate throughout deposition of the T_a divisions. This suggests that they were deposited from a part of the

turbidity current that had increasing C_v as the flow passed the study site. Thus, observed grain size variations have implications for the temporal and lateral evolution of the turbidity currents.

Lateral and/or temporal increase of C_v in turbidity currents could be a result of net erosion of underlying beds, collapse of the flow that was more rapid than sedimentation, or a combination of both processes. Rip-up clasts were not present in sandstones from the sampled core, siltstones showed minimal evidence of scour, and there was no evidence of amalgamation within T_a divisions suggesting that erosion did not contribute significantly to flow evolution at this location. These suggest that lateral and/or temporal increases in C_v in turbidity currents was a result of collapsing flow. Also, particle sedimentation rate from the lower region of the flow to the bed must have been slow relative to flow collapse.

Zircon and feldspar particles found in capping siltstones have similar Stokes settling velocities. This suggests that the overlying siltstones were deposited when local C_v in the depositional region was low. This could be a consequence of lateral and temporal density stratification within the flow. Variation of zircon and feldspar grain sizes between the underlying structureless sandstones and the overlying siltstones suggest that at later stage of the turbidity currents, C_v decreased dramatically. Feldspar grains in the overlying siltstone region were finer when compared to the underlying sandstones. This suggests that zircon grains behave as hydraulically fine grains in this region. Consequently, it can be inferred that, within this upper region, the particle volumetric concentration was low.

CHAPTER IV

SILTSTONE ELEMENTAL COMPOSITIONS: A PROXY FOR EROSIONAL

EVENT SIZES, BRUSHY CANYON FORMATION, WEST TEXAS AND SOUTH

NEW MEXICO

4.1 INTRODUCTION AND BACKGROUND

Geochemical properties have long been used to reconstruct histories of eolian

sediments (e.g., Glaccum and Prospero, 1980; Jaenicke and Schütz, 1978; Schnetger et

al., 2000; Shaw et al., 1974; Ver Straeten et al., 2011). The chemical composition of

detrital sediments is mainly controlled by the mineralogy of the source rocks, the

weathering regime, and the reactivity of the weathering products during transport

(Mackenzie, 2005). In a study of late-Holocene sediments of Gormire Lake, UK,

cyclical peaks of lithogenic elements (Si, Ti, K, Rb, Sr, Zr) covaried with peaks in Zr/Ti

ratio (Oldfield et al., 2003). These results were interpreted as episodes of enhanced

eolian input due to erosion following deforestation. Roy et al. (2013) studied

hydrological changes in the Chihuahua Desert, Mexico and interpreted that the supply of

Ti-bearing minerals associated with periods of summer precipitation and the abundance

of Zr-bearing minerals reflected periods of eolian input. Zr/Ti ratio was then used as a

proxy for eolian intensity. Similar interpretations were found in a study of changes in

tropical African climate by Brown et al. (2007). Peaks in Zr/Ti ratio were interpreted as

abrupt shifts to windy conditions. A combination of inorganic geochemical composition

and varve thickness was used as a proxy for interpreting the depositional history of the

northeastern Arabian Sea, Pakistan (Lückge et al., 2001). Increased lamination thickness and elevated Zr/Al and Ti/Al ratios were interpreted as evidence for increased eolian event size. Similar interpretations of a relationship between eolian activity and varve thickness and detrital flux were drawn in other studies (e.g., Dean et al., 2002; Hu et al., 1999). All of these studies proposed similar models in which high Zr/Ti ratio and lamination thickness are associated with periods of intense eolian activity.

In a study of volcanically derived dust in the deep sea, Shaw et al. (1974) proposed a model relating volcanic dust particle size to distance from source. The predicted traveled distance before deposition varied with particle size and height of the eruptive cloud. Fine particles from high eruptive clouds tended to travel the furthest. Ver Straeten et al. (2011) used grain sizes, elemental ratios, total organic content, and degree of bioturbation as proxies for interpreting depositional sequences and system tracts of black shales and limestones of the Oatka Creek Formation in the Devonian Appalachian Basin. Al was commonly found in clay minerals and was used as a proxy for fine-grained sediments. Si, Zr, and Ti were related to coarser sediments. Thus, high Si/Al, Zr/Al and Ti/Al ratios reflected sand-sized sediment input. A decrease in any of these elemental ratios was associated with deposition in distal and basinal environments. In this model, heavy elements were size sorted along the travel path. Zr was enriched in silt to fine sand and Ti was associated with clay (Oldfield et al., 2003). In other words, high Zr/Ti ratio was related to coarsening sediment input. Thus, a combination of high Zr/Ti ratio and coarse-grained particles indicated sedimentation in relatively proximal depositional environments.

In summary, there are two different proposed models to explain fluctuations in Zr/Ti ratio (1) high Zr/Ti ratio and lamination thickness are associated with periods of intense eolian activity or (2) a combination of high Zr/Ti ratio and coarse-grained particles indicated sedimentation in relatively proximal depositional environments. This research focuses on the potential driving mechanisms for variations in Zr/Ti fluorescence ratio and in laminated siltstones of the Brushy Canyon Formation.

The proposed transportational and depositional models of this rock unit are divided into two groups—eolian dust and low-density turbidity currents. The differences between fluvial and eolian deposits are not investigated in this study.

The unit chosen for study is the gray fine to medium grained thinly laminated siltstones and sandy siltstones of the Brushy Canyon Formation in the Delaware Mountain Group. Sedimentary rocks of the Delaware Mountain Group sediments have been interpreted as deposits from dual density flows, where saline density currents deposited sands and less-dense currents deposited detrital silt and organic materials (Harms and Williamson, 1988). Light gray laminae were coarser and organic-poor whereas darker gray laminae were finer and organic-rich (Fischer and Sarnthein, 1988; Harms and Williamson, 1988; Williamson, 1980). Siltstone was deposited from suspension without any influence from the bottom currents because the siltstone was (1) draping as a laterally continuous and uniform blanket, (2) lacking current structures, (3) rich in organic matter, and (4) each lamina was individually graded, increasing in organic content upward (Harms and Williamson, 1988; Williamson, 1980). Silver and Todd (1969) and Beaubouef et al. (1999) proposed a similar model that the Delaware

Mountain Group was deposited from turbidity currents during a period of low sea level. Thus, abundant sediments were transported into the basin by sediment-gravity flows. High-density turbidity currents generated channel filling sandstones while laminated siltstones were deposited from dilute, low-density turbidity currents (Beaubouef et al., 1999).

On the other hand, Fischer and Sarnthein (1988) proposed an eolo-marine or wind-transported but water-laid model for the deposition of the Delaware Mountain Group because (1) the paucity of clay found in the deposits suggested an eolian origin, (2) fallout of windblown dust could create topographically draping beds of laminated siltstones, and (3) these deposits were similar to Pleistocene paraglacial deposits of the Sahara. In this model, sands were transported by eolian dunes and fine sand, silt, and clay were transported as dust. Deposition of sand wedges at the shelf break during low sea level generated turbidity currents and, consequently, channel filling sand bodies. Fine sand and silt were deposited as hemipelagic laminated siltstones. Paleogeography study proposed that during Permian time, the Delaware basin was located in the trade-wind belt of the northern hemisphere (Fischer and Sarnthein, 1988). Fine sand, silt, and clay were transported as wind-blown dust (Adams, 1936) by strong trade-wind periods (Fischer and Sarnthein, 1988). Compositions of detrital feldspar suggest that the source areas were the Rockies and other nearby uplifts (Hull, 1957).

Although Silver and Todd (1969), Williamson (1980), Fischer and Sarthein (1988), Harms and Williamson (1988) and Beaubouef et al. (1999) proposed different models of transportation of the Delaware Mountain Group sediments, their findings

unanimously agreed upon mode of deposition of the thinly laminated siltstones. This lithology topographically draped preexisting layers and was deposited from suspension with little or low disruption or alteration by bottom currents. The rock unit was deposited from dilute suspensions as fine-grained turbidity currents, hemipelagites, or both. Therefore, particles in these laminated siltstones were hydraulically equivalent at infinitely dilute suspensions. This allows a detailed investigation on particle size and density variation. Also, mineral distribution and sedimentary rock structures were not affected by bottom currents allowing accurate measurement of lamina thickness. Consequently, these thinly laminated siltstones form an ideal test unit for identifying sources of variation in Zr/Ti ratio.

4.2 METHODS OF STUDY

Fifteen thinly laminated siltstones hand samples were collected from three measured sections from the Upper Brushy Canyon Formation, Guadalupe Mountains National Park, west Texas. The measured sections came from thinly laminated siltstone outcrops overlying a prominent structureless sandstone bed representing late-stage channel fill in a large channel body exposed on Salt Flat Bench (Fig. 4.1). X-ray fluorescence analytical microscopy, µXRF, was used to map elemental distribution in slabbed hand samples. Scans were conducted at 10 µm resolution to detect and characterize individual grains; two to four 10 µm resolution scans were conducted from the base to the top of each sample.
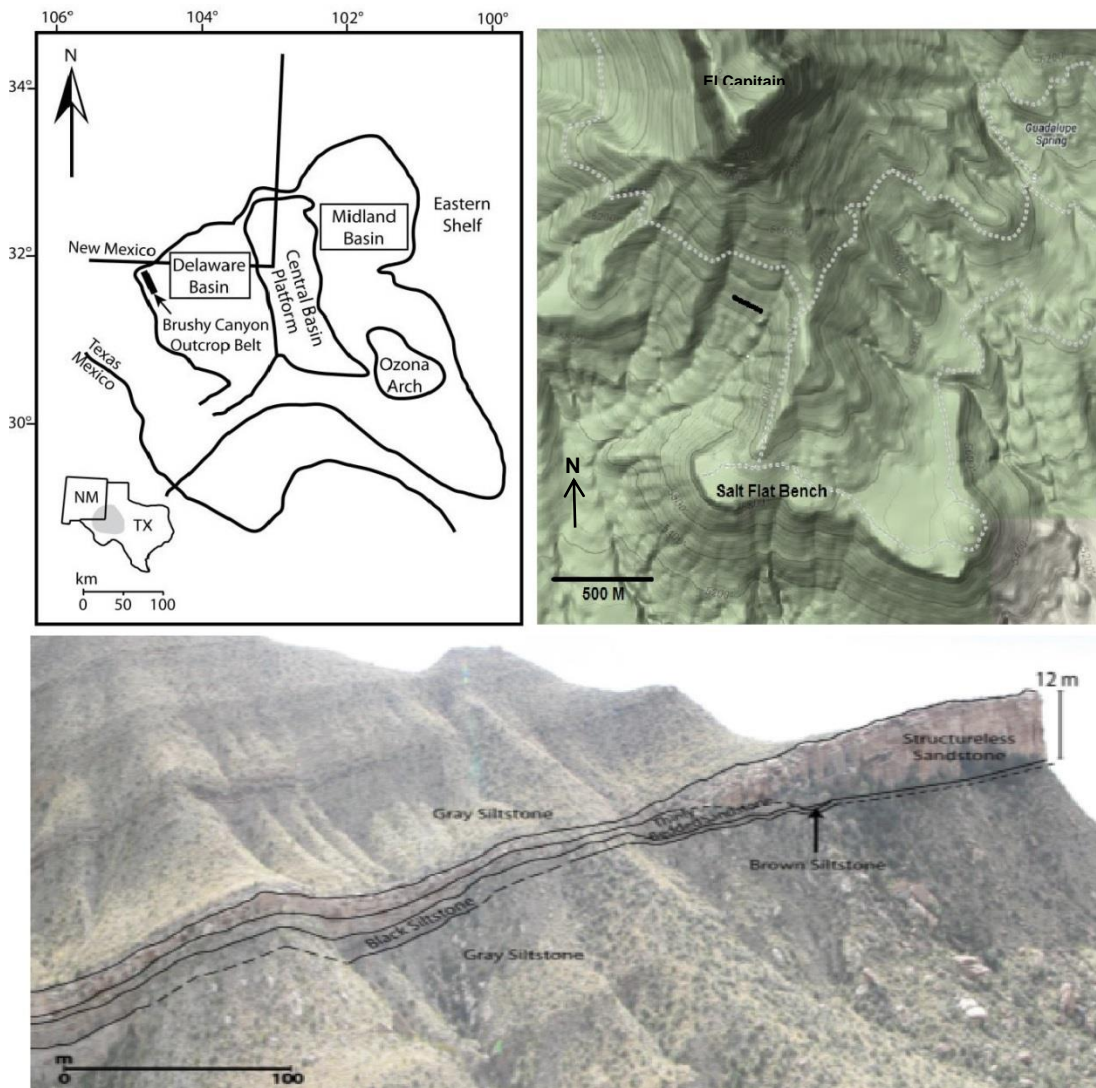
Figure 4.1 A prominent structureless sandstone bed exposed on Salt Flat Bench (vertically exaggerated outcrop photo to show different deposits). The measured sections came from thinly laminated siltstone outcrops (Gray Siltstone) overlying this late-stage channel filling structureless sandstone. The sampling location's GPS coordinates: N 31.871, W 104.858. Modified from Gunderson (2011).

4.3 RESULTS

4.3.1 Zircon and Rutilated Quartz Concentrations and Distributions

Zircon and rutilated quartz grain sizes were log-normally distributed (Fig. 4.2) with sample standard deviation < 0.35 ϕ (very well-sorted). In every scanning location, rutilated quartz grains were systematically larger than zircon grains (Fig. 4.3). Zircon grains were silt-sized, and rutilated quartz grains were very fine sand-to coarse silt-sized. Additionally, rutilated quartz grain sizes were positively correlated ($r = 0.771$) with those of zircon grains (Fig. 4.3). This correlation is consistent with the hypothesis that they were sorted together during deposition from suspension and that they are hydraulically equivalent at the time of deposition. Consequently, the average density of rutilated quartz can be estimated by balancing Stokes settling velocity of rutilated quartz with that of zircon.

$$\left(\frac{d_{Zr}}{d_{Ti}}\right)^2 = \frac{\rho_{Ti}-\rho}{\rho_{Zr}-\rho} \tag{4.1}$$

The above equation can be rewritten in the following linear form of

$$\phi_{Ti} = \phi_{Zr} + \frac{1}{2}\log_2\left(\frac{\rho_{Ti}-\rho}{\rho_{Zr}-\rho}\right). \tag{4.2}$$

Here, d_{Zr} and d_{Ti} represent zircon and rutilated quartz diameters. ρ, ρ_{Zr}, and ρ_{Ti} are densities of fluid, zircon, and rutilated quartz, respectively. ϕ_{Zr} and ϕ_{Ti} represent zircon

and rutilated quartz grain size in phi-scale. The regression line between quartz and

zircon grain sizes had a slope of 1.1 ± 0.3 (Fig. 4.3) but the slope's interception $\neq 0$.

Therefore, the densities of these minerals were not equal to each other. These minerals

were hydraulically equivalent, and the density of rutilated quartz was calculated by

equating settling velocity of zircon to that of quartz particle. Rutilated quartz grains had

an average estimated density of 3.34 ± 0.05 g cm^{-3} (standard error from 36

measurements), suggesting an average rutile content of 43% by volume.

There is no significant correlation between Zr/Ti fluorescence ratio and either

zircon or rutilated quartz grain sizes (Fig. 4.4, 4.5). In other words, variations in Zr/Ti

ratio were not caused by variations in mineral grain size.
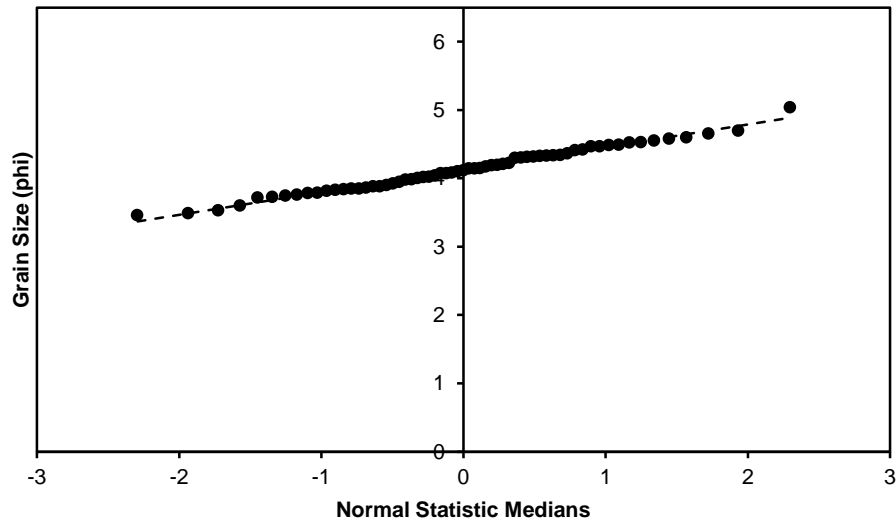
Figure 4.2 Normal probability plots of rutilated quartz grain sizes from small scans

show that these grains are normally distributed ($R^2 = 0.988$; $p = 10^{-33}$).
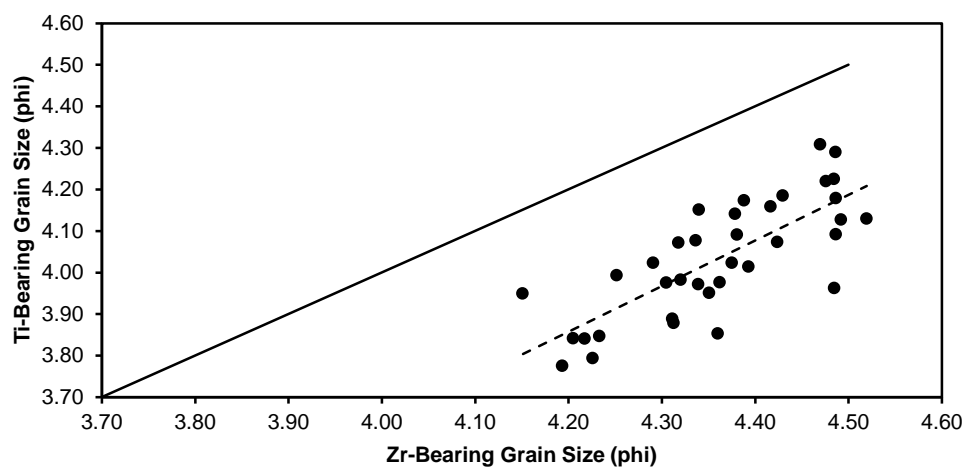
Figure 4.3 Rutilated quartz grain size (phi) with respect to zircon grain size (phi) from each 10 µm resolution scanning location is shown in •. A line of 1:1 grain size ratio is displayed in —. Linear regression line (- - -) has a slope of 1.098 ± 0.316 (95% confidence) and *p*-value of 10^{-8}.
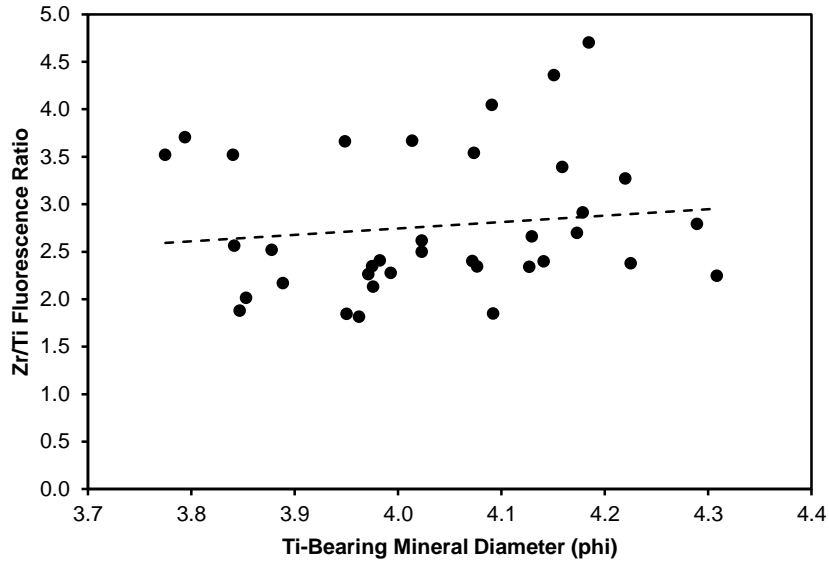
Figure 4.4 Zr/Ti fluorescence ratio with respect to Ti-rich mineral grain size (phi) ($R^2 =$ 0.016; p for the regressed slope 0.489).
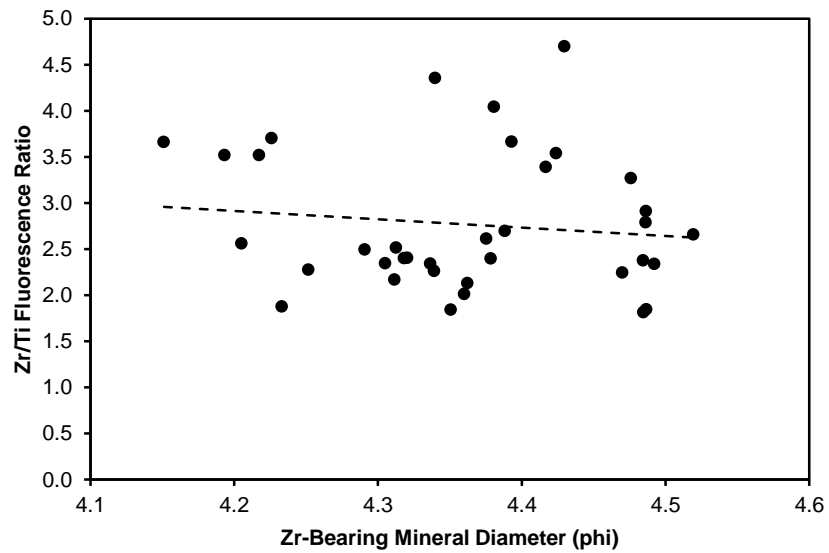
Figure 4.5 Zr/Ti fluorescence ratio with respect to Zr-rich mineral grain size (phi) ($R^2 =$ 0.014; p for the regressed slope = 0.472).

4.3.2 Lamination Thickness

Alternating light gray laminae and darker gray/black laminae were horizontal and parallel to each other. Black laminae were enriched in Fe (Fig. 4.6) allowing consistent estimation of lamination thickness from 10 µm resolution XRF scans. All samples showed positive correlations (positive r-value; Table 4.1; Fig. 4.7), and nine of fifteen samples had significant linear relationship between lamination thickness and Zr/Ti ratio ($p < 0.05$; Table 4.1). The remaining samples showed no significant relationship at the 95% confidence level; no negative correlations were observed.

Results from this research found that (1) both zircon and rutilated quartz grains were well-sorted and normally distributed, (2) rutilated quartz grain sizes were systematically correlated with zircon grain sizes, (3) neither zircon grain nor rutilated quartz grain size correlated with Zr/Ti ratio, and (4) lamination thickness and Zr/Ti fluorescence ratio had positive correlations.

Table 4.1 Linear regression and correlation analysis between lamination thickness and Zr/Ti ratio. Lamination thickness and Zr/Ti ratio are positively correlated in every sample.

Sample	Slope	P-value of the Slope	Correlation r-value
1-3	0.152	**0.007***	0.853
1-4	0.232	**0.003***	0.863
1-5	0.087	0.273	0.402
1-6	0.223	**0.018***	0.940
1-7	0.085	0.089	0.638
1-8	0.311	**0.040***	0.831
1-9	0.081	0.310	0.338
2-1	0.095	**0.012***	0.648
2-2	0.160	**0.039***	0.626
2-3	0.107	0.320	0.443
3-1	0.065	0.185	0.485
3-2	0.119	0.050	0.754
3-3	0.126	**0.017***	0.799
3-4	0.062	**0.034***	0.670
3-5	0.214	**0.002***	0.872

[*]Sample with linear regression between Zr/Ti fluorescence ratio and lamination thickness at the 95% confidence interval or greater shown in bold.

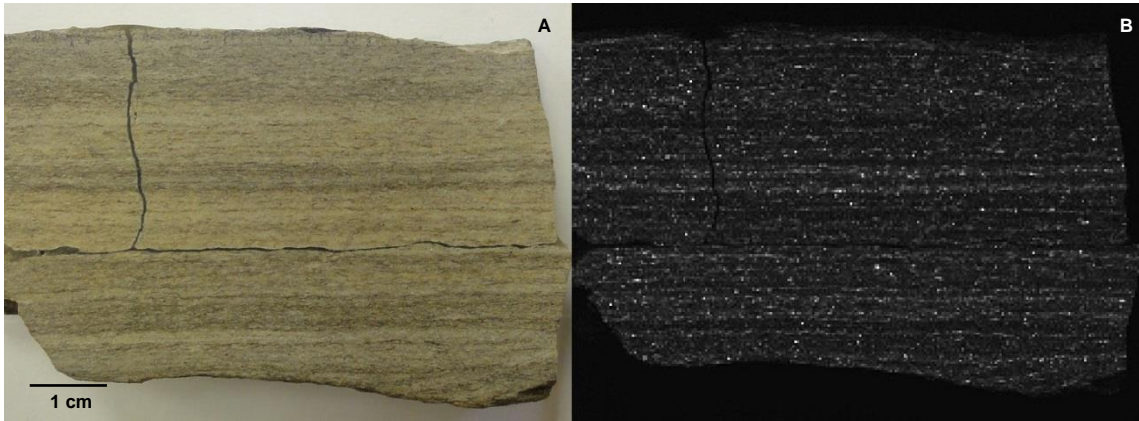**Figure 4.6** Fe-rich bands occur along black laminae. A) MBC 1-5 rock sample. B) Fe-fluorescence of MBC 1-5 rock sample.
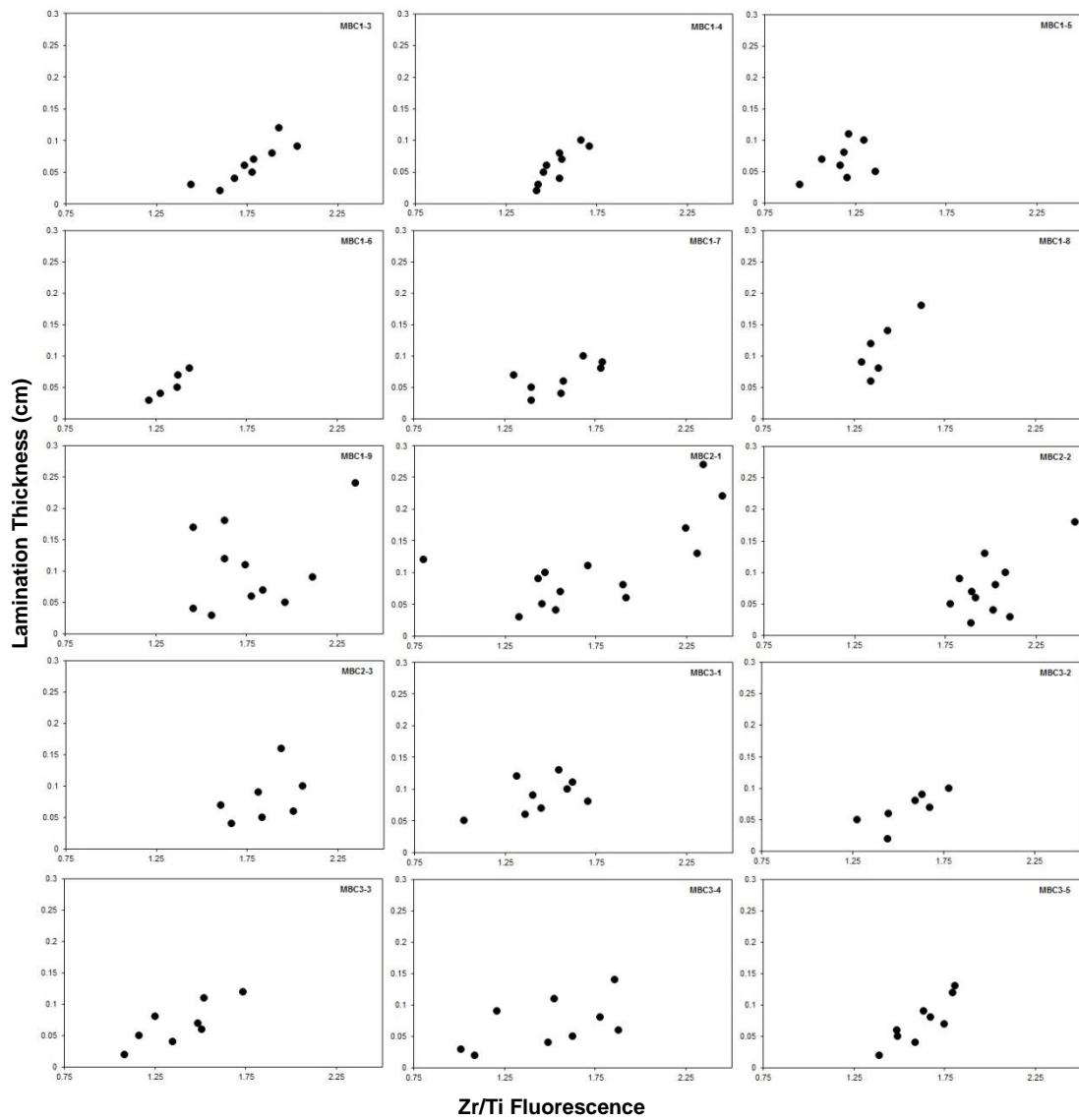
Figure 4.7 Correlation plots of lamination thickness and Zr/Ti fluorescence ratio. All samples have positive correlation.

4.4 ANALYSIS AND DISCUSSION

4.4.1 Sources of Zr/Ti Ratio Variation

Particles' susceptibility to movement is highly influenced by grain size, shape, packing, and sorting, and initial grain entrainment results from fluid drag and lift forces on more exposed grains (Nickling, 1988). In a series of wind-tunnel experiments of dry loose sand-sized sediments of a range of grain sizes, as wind velocity was slowly increased, less exposed grains were moved by fluid drag force (Nickling, 1988). When particle to fluid density ratio is low, the initial particle motion occurs at low fluid velocity (Iversen et al., 1987). Thus, denser and smaller grains have lower susceptibility to initial movement and require a relatively higher critical shear velocity to initiate motion due to their lesser exposed surface area and higher particle to fluid density ratio.

Since zircon particles are smaller and denser than rutilated quartz particles (Fig. 4.3), zircon grains have lower susceptibility to particle movement. Variations in Zr/Ti ratio are not correlated to grain size of either mineral (Fig. 4.4, 4.5). These observations suggest that changes in Zr/Ti ratio did not result from varying in mineral grain sizes but were likely from variations in mineral abundance. Consequently, high Zr/Ti ratios were from increases in zircon abundance likely related to periods of enhanced erosion where fluid speeds were high enough to move particles with lower susceptibility to movement. Thicker lamination associated with high Zr/Ti ratio (Fig. 4.7); this is consistent to results from Hu et al. (1999), Lückge et al. (2001), and Dean et al. (2002). Therefore, variations in Zr/Ti ratio are, therefore, most likely derived from fluctuations in intensity of erosional events.

4.5 CONCLUSIONS

Erosional event size during the deposition of thinly laminated siltstone in the Brushy Canyon Formation was qualitatively analyzed from physical properties of zircon and rutilated quartz. Zircon grains were systematically finer than rutilated quartz grains but neither of these grain sizes was correlated with Zr/Ti fluorescence ratio. Also, Zr/Ti fluorescence ratio and lamination thickness had positive correlations. Therefore, fluctuations in Zr/Ti ratio were derived from changes in erosional intensity. The grain-size distribution of these rock samples should be further analyzed in order to classify the modes of transportation and deposition.

REFERENCES

Adams, J. E., 1936, Oil pool of open reservoir type: AAPG Bulletin, v. 20, no. 6, p. 780-796.

Allen, J. R. L., 1991, The Bouma division A and the possible duration of turbidity currents: Journal of Sedimentary Research, v. 61, no. 28, p. 291-295.

Amy, L. A., Talling, P. J., Edmonds, V. O., Sumner, E. J., and Lesueur, A., 2006, An experimental investigation of sand-mud suspension settling behaviour: implications for bimodal mud contents of submarine flow deposits: Sedimentology, v. 53, no. 6, p. 1411-1434.

Bagnold, R. A., 1962, Auto-suspension of transported sediment: turbidity currents: Proceedings of the Royal Society of London. Series A, Mathematical and Physical Sciences, v. 265, no. 1322, p. 315-319.

Beaubouef, R. T., Rossen, C., Zelt, F. B., Sullivan, M. D., Mohrig, D. C., and Jennette, D. C., 1999, Deep-water sandstones, Brushy Canyon Formation, west Texas, AAPG Hedberg Field Research Conference.

Berthault, G., 1988, Experiments on lamination of sediments: EN Technology Journal, v. 3, p. 25-29.

Bouma, A. H., 1962, Sedimentology of some flysch deposits: a graphic approach to facies interpretation, Amsterdam, Flsevier.

Bowen, A. J., Normark, W. R., and Piper, D. J. W., 1984, Modelling of turbidity currents on Navy Submarine Fan, California Continental Borderland: Sedimentology, v. 31, no. 2, p. 169-185.

Brown, E. T., Johnson, T. C., Scholz, C. A., Cohen, A. S., and King, J. W., 2007, Abrupt change in tropical African climate linked to the bipolar seesaw over the past 55,000 years: Geophysical Research Letters, v. 34, no. 20, p. L20702.

Chhabra, R. P., Agarwal, S., and Chaudhary, K., 2003, A note on wall effect on the terminal falling velocity of a sphere in quiescent Newtonian media in cylindrical tubes: Powder Technology, v. 129, no. 1, p. 53-58.

Davies, R., 1968, The experimental study of the differential settling of particles in suspension at high concentrations: Powder Technology, v. 2, no. 1, p. 43-51.

Davis, H., R., Birdsell, and H., K., 1988, Hindered settling of semidilute monodisperse and polydisperse suspensions, Hoboken, NJ, Wiley-Blackwell.

Dean, W. E., Forester, R. M., and Bradbury, J. P., 2002, Early Holocene change in atmospheric circulation in the Northern Great Plains: an upstream view of the 8.2 ka cold event: Quaternary Science Reviews, v. 21, no. 16, p. 1763-1775.

Di Felice, R., 1996, A relationship for the wall effect on the settling velocity of a sphere at any flow regime: International Journal of Multiphase Flow, v. 22, no. 3, p. 527-533.

Felix, M., 2002, Flow structure of turbidity currents: Sedimentology, v. 49, no. 3, p. 397-419.

Fischer, A. G., and Sarnthein, M., 1988, Airborne silts and dune-derived sands in the
Permian of the Delaware Basin: Journal of Sedimentary Research, v. 58, no. 4, p.
637-643.

Glaccum, R. A., and Prospero, J. M., 1980, Saharan aerosols over the tropical North
Atlantic: mineralogy: Marine Geology, v. 37, no. 3, p. 295-321.

Gunderson, S., 2011, Early channel evolution in the Middle Permian Brushy Canyon
Formation, west Texas, USA. [Master] thesis, Texas A&M University, 35 p.

Harms, J. C., and Williamson, C. R., 1988, Deep-water density current deposits of
Delaware Mountain Group (Permian), Delaware Basin, Texas and New Mexico:
AAPG Bulletin, v. 72, no. 3, p. 299-317.

Haughton, P., Davis, C., McCaffrey, W., and Barker, S., 2009, Hybrid sediment gravity
flow deposits: classification, origin and significance: Marine and Petroleum
Geology, v. 26, no. 10, p. 1900-1918.

Hoyos, M., Bacri, J. C., Martin, J., and Salin, D., 1994, A study of the sedimentation of
noncolloidal bidisperse, concentrated suspensions by an acoustic technique:
Physics of Fluids, v. 6, no. 12, p. 3809-3817.

Hu, F., Slawinski, D., Wright, H., Ito, E., Johnson, R., Kelts, K., McEwan, R., and
Boedigheimer, A., 1999, Abrupt changes in North American climate during early
Holocene times: Nature, v. 400, no. 6743, p. 437-440.

Hull, J. P. D., 1957, Petrogenesis of Permian Delaware Mountain sandstone, Texas and
New Mexico: AAPG Bulletin, v. 41, no. 2, p. 278-307.

Iversen, J. D., Greeley, R., Marshall, J. R., and Pollack, J. B., 1987, Aeolian saltation threshold: the effect of density ratio: Sedimentology, v. 34, no. 4, p. 699-706.

Jaenicke, R., and Schütz, L., 1978, Comprehensive study of physical and chemical properties of the surface aerosols in the Cape Verde Islands region: Journal of Geophysical Research: Oceans, v. 83, no. C7, p. 3585-3599.

Julien, P. Y., 1998, Erosion and Sedimentation, Cambridge, Cambridge University Press.

Julien, P. Y., and Lan, Y., 1991, Rheology of hyperconcentrations: Journal of Hydraulic Engineering, v. 117, no. 3, p. 346-353.

Kneller, B. C., and McCaffrey, W. D., 2003, The interpretation of vertical sequences in turbidite beds: the influence of longitudinal flow structure: Journal of Sedimentary Research, v. 73, no. 5, p. 706-713.

Komar, P. D., 1985, The hydraulic interpretation of turbidites from their grain sizes and sedimentary structures: Sedimentology, v. 32, no. 3, p. 395-407.

Lowe, D. R., 1982, Sediment gravity flows II: depositional models with special reference to the deposits of high-density turbidity currents: Journal of Sedimentary Research, v. 52, no. 1, p. 279-297.

Lückge, A., Doose-Rolinski, H., Khan, A. A., Schulz, H., and von Rad, U., 2001, Monsoonal variability in the northeastern Arabian Sea during the past 5000 years: geochemical evidence from laminated sediments: Palaeogeography, Palaeoclimatology, Palaeoecology, v. 167, no. 3, p. 273-286.

Machač, I., and Lecjaks, Z., 1995, Wall effect for a sphere falling through a non-Newtonian fluid in a rectangular duct: Chemical Engineering Science, v. 50, no. 1, p. 143-148.

Mackenzie, F. T., 2005, Sediments, diagenesis, and sedimentary rocks: treatise on geochemistry, Elsevier Science.

Middleton, G. V., 1976, Hydraulic interpretation of sand size distributions: The Journal of Geology, v. 84, no. 4, p. 405-426.

Middleton, G. V., and Southard, J. B., 1984, Mechanics of sediment movement.

Mulder, T., and Alexander, J., 2001, The physical character of subaqueous sedimentary density flows and their deposits: Sedimentology, v. 48, no. 2, p. 269-299.

Nickling, W., 1988, The initiation of particle movement by wind: Sedimentology, v. 35, no. 3, p. 499-511.

Nicolai, H., Herzhaft, B., Hinch, E. J., Oger, L., and Guazzelli, E., 1995, Particle velocity fluctuations and hydrodynamic self-diffusion of sedimenting non-Brownian spheres: Physics of Fluids, v. 7, no. 1, p. 12-23.

Oldfield, F., Wake, R., Boyle, J., Jones, R., Nolan, S., Gibbs, Z., Appleby, P., Fisher, E., and Wolff, G., 2003, The late-Holocene history of Gormire Lake (NE England) and its catchment: a multiproxy reconstruction of past human impact: The Holocene, v. 13, no. 5, p. 677-690.

Richardson, J. F., and Meikle, R. A., 1961, Sedimentation and fluidisation part III: the sedimentation of uniform fine particles and of two-component mixtures of solids: Transactions of the Institution of Chemical Engineers, v. 39, p. 348-356.

Richardson, J. F., and Zaki, W. N., 1954, Sedimentation and fluidisation: Part I:

    Transactions of the Institution of Chemical Engineers, v. 32, p. S82-S100.

Riley, N. A., 1941, Projection sphericity: Journal of Sedimentary Research, v. 11, no. 28,

    p. 94-95.

Roy, P. D., Rivero-Navarette, A., Lopez-Balbiaux, N., Pérez-Cruz, L. L., Metcalfe, S.

    E., Sankar, G. M., and Sánchez-Zavala, J. L., 2013, A record of Holocene

    summer-season palaeohydrological changes from the southern margin of

    Chihuahua Desert (Mexico) and possible forcings: The Holocene, v. 23, no. 8, p.

    1105-1114.

Rubey, W. W., 1933, The size distribution of heavy minerals within a water-laid

    sandstone: Journal of Sedimentary Research, v. 3, no. 1, p. 3-29.

Schnetger, B., Brumsack, H. J., Schale, H., Hinrichs, J., and Dittert, L., 2000,

    Geochemical characteristics of deep-sea sediments from the Arabian Sea: a high-

    resolution study: Deep Sea Research Part II: Topical Studies in Oceanography, v.

    47, no. 14, p. 2735-2768.

Segre, N., P., Liu, F., Umbanhowar, P., Weltz, and A., D., 2001, An effective

    gravitational temperature for sedimentation: Nature, v. 409, no. 6820, p. 594-597.

Shaw, D. M., Watkins, N. D., and Huang, T. C., 1974, Atmospherically transported

    volcanic glass in deep-sea sediments: theoretical considerations: Journal of

    Geophysical Research, v. 79, no. 21, p. 3087-3094.

Silver, B. A., and Todd, R. G., 1969, Permian cyclic strata, northern Midland and
    Delaware Basins, west Texas and southeastern New Mexico: AAPG Bulletin, v.
    53, no. 11, p. 2223-2251.

Slingerland, R., and Smith, N. D., 1986, Occurrence and formation of water-laid placers:
    Annual Review of Earth and Planetary Sciences, v. 14, no. 1, p. 113-147.

Slingerland, R. L., 1977, The effects of entrainment on the hydraulic equivalence
    relationships of light and heavy minerals in sands: Journal of Sedimentary
    Research, v. 47, no. 2, p. 753-770.

Steidtmann, J. R., 1982, Size-density sorting of sand-size spheres during deposition from
    bedload transport and implications concerning hydraulic equivalence:
    Sedimentology, v. 29, no. 6, p. 877-883.

Van Tassell, J., 1981, Silver abyssal plain carbonate turbidite: flow characteristics: The
    Journal of Geology, v. 89, no. 3, p. 317-333.

Ver Straeten, C. A., Brett, C. E., and Sageman, B. B., 2011, Mudrock sequence
    stratigraphy: a multi-proxy (sedimentological, paleobiological and geochemical)
    approach, Devonian Appalachian Basin: Palaeogeography, Palaeoclimatology,
    Palaeoecology, v. 304, no. 1, p. 54-73.

Visher, G. S., 1969, Grain size distributions and depositional processes: Journal of
    Sedimentary Research, v. 39, no. 3, p. 1074-1106.

Williamson, C. R., 1980, Sedimentology of Guadalupian deep-water clastic facies,
    Delaware Basin, New Mexico and west Texas: New Mexico Geological Society
    Guidebook, v. 31st Field Conference, p. 195-204.